RESEARCH ARTICLE | SEPTEMBER 10 2026

A numerical study on the dynamics of non-inertial and inertial particles in geophysical flows

Nishanta Baral ; Eric Forgoston ; M. Ani Hsieh

Chaos 36, 093125 (2026)
https://doi.org/10.1063/5.0323103

Chaos ARTICLE pubs.aip.org/aip/cha

A numerical study on the dynamics of non-inertial and inertial particles in geophysical flows

Cite as: Chaos 36, 093125 (2026); doi: 10.1063/5.0323103
Submitted: 15 January 2026 · Accepted: 3 August 2026 ·
Published Online: 10 September 2026

View Online Export Citation CrossMark

Nishanta Baral,[1] Eric Forgoston,[1,a)] and M. Ani Hsieh[2]

AFFILIATIONS

[1]School of Computing, Montclair State University, Montclair, New Jersey 07043, USA
[2]Department of Mechanical Engineering and Applied Mechanics, University of Pennsylvania, Philadelphia, Pennsylvania 19104, USA

[a)]**Author to whom correspondence should be addressed:** eric.forgoston@montclair.edu

ABSTRACT

We consider the dynamics of non-inertial and inertial particles in several types of geophysical flows. The underlying structures of the flow fields are examined via their associated Lagrangian coherent structures, which are found by computing the finite-time Lyapunov exponent (FTLE) field. For inertial particles with finite size and mass, the Maxey–Riley equation is used to describe the particles' motion and to find the inertial FTLE field. We compare the behavior and FTLE fields of massless non-inertial particles and light (bubbles) and heavy (aerosols) inertial particles using the velocity fields from the double-gyre flow, Bickley jet, and eddy-quadrupole models, as well as an ocean dataset of Monterey Bay, California. In addition, we explore the preferential aggregation of inertial particles in these flows and show that inertia affects particle transport: aerosols accumulate along maximal FTLE ridges, and bubbles cluster inside vortex cores, where the clustering depends on the density ratio and the Stokes number. Inclusion of the Coriolis force further influences the dynamics via ejection of particles between cyclonic and anticyclonic structures, where the rate of aggregation onto these rotational attractors increases with the strength of rotation. We also study the validity of ignoring the Faxén correction and an often used assumption whereby the material derivative is set equal to the total derivative. The Faxén correction has a negligible effect for these flows, while the material derivative simplification changes the timescale on which inertial particles aggregate onto their attractors.

The transport of particles by oceanic and atmospheric flows is crucial in understanding various biological and physical phenomena, such as air quality, marine ecosystems, spread of pollutants and other contaminants, and different mixing processes. This transport is governed by dynamic fluid-flow structures, which can be quantified by computing the Lagrangian coherent structures (LCSs). Typically, LCSs are identified using passive fluid tracers, yet many physically and biologically relevant particles possess finite size and mass, and, therefore, these inertial particles do not follow the same trajectories as non-inertial passive tracers. In this work, we investigate the transport of inertial particles in geophysical flows by using the Maxey–Riley (MR) equation to identify the corresponding inertial LCS. Using a variety of flow models and ocean velocity data, we explore how particle density and Stokes number influence inertial particle aggregation. We further examine the influence of common assumptions in the study of inertial particle dynamics and quantify their impact on material transport.

I. INTRODUCTION

The study of oceanic and atmospheric circulation is crucial for understanding a wide range of phenomena, such as weather and climate patterns,[1,2] marine ecosystems,[3] and the transport of contaminants.[2,4–6] In particular, the atmospheric transport of particles (contaminants, dust, or other materials) is driven by atmospheric circulation patterns and can range from spanning a localized area to entire continents.[6] A few notable examples include: (a) an intense dust-storm located over the Gobi desert on April 19, 1998, which crossed the Pacific Ocean in five days and settled along the mountain ranges between the province of British Columbia in Canada and the state of California in the United States of America (USA),[5,7] (b) during the 1970s and 1980s, lead isotopes originating from Europe were transported southward to Africa and then westward via trade winds to the island of Barbados in the Lesser Antilles,[7] (c) hurricane Ivan transported soybean rust from South America to the Gulf coast of the USA,[4] and (d) recently, in 2024, wildfire smoke originating in Western Canada traveled east, affecting air quality in eastern Canada and along the USA's East Coast, before crossing the North Atlantic to western Europe.[8]

Similarly, ocean circulation plays a key role in material transport, with two significant examples being the Gulf Stream transport and the Antarctic Circumpolar Current (ACC). Material transport across the Gulf Stream is critical for the North Atlantic climate, as it drives mixing processes that influence sea surface temperature and chlorophyll levels.[9] Likewise, the ACC is the driving force for air–sea exchanges of heat, freshwater, and atmospheric trace gases, having a profound impact on global climate.[10] Thus, the study of material transport in both atmospheric and oceanic flows is of immense research interest, with the goal of improving accurate forecasting and prediction in real-world scenarios, such as oil spill dispersion,[11–13] oceanic rubbish transport,[12,14,15] and the advection of airborne micro-organisms by atmospheric flows.[1,4]

While direct numerical simulation of the Navier–Stokes equations enables accurate prediction of material transport, identifying the underlying coherent structures within the flow is needed to interpret and understand the patterns of material transport. Specifically, Lagrangian coherent structures (LCSs) are of great importance since they can quantify material transport by providing a skeleton of fluid flow.[11,12] The study of coherent structures has proven valuable across various fields. For example, LCSs in the ocean act as barriers between recirculation zones within a bay and the open ocean. In Monterey Bay, LCSs have a dominant period of 8–9 days, which is critical for understanding long-term particle transport.[16] Pollutants released on one side of an LCS may recirculate within the bay, while those released on the other side can quickly escape to the open ocean. Another well-known example involves the use of LCS to understand the spread of oil during the aftermath of the Deepwater Horizon explosion.[11–13] Beyond oceanography, the study of LCS has proven valuable in atmospheric science,[17] engineering,[18] pollution reduction,[18] population dynamics,[19] vehicle loitering,[2] path planning,[20,21] and wave propagation.[22]

LCSs, which extend stable and unstable manifolds to time-dependent systems, describe the most repelling, attracting, and shearing material surfaces in a flow field.[11,23,24] This allows for a simpler understanding of flow topology, a more accurate comprehension of material transport, and the potential to predict large-scale flow patterns and mixing events.[11] In two-dimensional (2D) flows, LCSs act as one-dimensional (1D) separating boundaries, and are analogous to ridges defined by local maximum instability, which can be quantified using finite-time Lyapunov exponents (FTLEs).[11,25]

Over the past few decades, numerous studies have explored LCSs to better understand their role in a variety of atmospheric and oceanic flows. In addition, unmanned aerial vehicles (UAVs), autonomous underwater vehicles (AUVs), and autonomous surface vehicles (ASVs) have been employed to track LCSs and utilize this knowledge for a wide array of sensing tasks.[1,2,4,25–27] The use of these unmanned sensors has enhanced our knowledge of ocean dynamics, thereby improving our understanding of ocean ecosystems, weather patterns, and climate prediction. For example, UAVs are used to track coherent structures in the atmosphere, aiding the prediction of pathogen distribution patterns.[4] Similarly, AUVs and ASVs track coherent structures in oceanic flows, providing valuable insights into various phenomena, such as temperature, salinity, and density measurements.[2] These technologies have also contributed to the study of biological events like phytoplankton clustering and algal blooms.[28]

Importantly, the tracking and sensing strategies mentioned above have been derived using highly abstracted kinematic models that neglect the effects of shape and inertia due to the finite size and mass of the vehicle or sensor. Most existing techniques for extracting and analyzing coherent structures are limited to point particles that are neutrally buoyant. The standard LCS computation via FTLEs describes the transport of infinitesimal, massless objects. Since finite-size particles with mass do not follow the same trajectories, one must instead compute inertial FTLEs (iFTLEs) to find inertial LCSs, which describe the transport of inertial particles.

The inertia of particles leads to clustering and dispersion, with fluid particles preferentially aggregating in regions of low vorticity.[29] For example, Beron-Vera *et al.*[30] showed that the inertia of drifters plays a key role in its accumulation within the subtropical ocean gyres. Even microplastics exhibit inertial effects, as experimentally demonstrated by the dependence of particle settling velocities on both flow inertia and particle shape.[31] Furthermore, studies on the movement of inertial prey particles in jellyfish-generated flows revealed that prey with inertia and escape forces exhibit smaller capture regions compared to infinitesimal prey, with those near the boundaries of the capture region being more likely to evade capture.[32] Therefore, in this article, we will investigate the interplay between inertial effects and transport in a variety of geophysical flows. We will use the Maxey–Riley (MR) equation to generate velocity fields for inertial particles and show how the FTLEs and iFTLEs differ for each flow as a function of particle density ratio and Stokes number. We will also perform studies of how particles aggregate relative to the LCSs for different parameter values. Last, we undertake a study of the effect of several assumptions often made with regard to the MR equation.

The analysis is developed incrementally, starting with a benchmark flow, extending to different kinematic models, and finally applying the framework to real ocean data. We begin with the necessary theoretical background in Sec. II, then analyze the double-gyre (DG) flow in Sec. III, which serves as a benchmark. We extend the analysis to two additional geophysical flow models, the Bickley jet in Sec. IV A, and the eddy-quadrupole flow in Sec. IV B. Last, we analyze ocean surface velocity data from Monterey Bay, California in Sec. V. Conclusions are discussed in Sec. VI.

II. THEORETICAL FRAMEWORK

A. Lagrangian coherent structures (LCSs)

As mentioned in the Introduction, LCSs are material lines that organize fluid-flow transport and may be viewed as the extensions of stable and unstable manifolds to general time-dependent systems.[23,24] LCSs can be studied by (a) identifying uniformly hyperbolic trajectories on a fixed portion of time and then growing their associated finite-time invariant manifolds, (b) constructing stable and unstable manifolds of fluid flows, or (c) deriving a measure of hyperbolic stretching and defining LCSs as the most hyperbolic structures.[33] The third approach is the most commonly used approach to study LCSs in the literature. A commonly used quantity to measure hyperbolic stretching is the FTLE,[17] which calculates the rate of separation between two nearby passive tracer particles over a finite time period.[22] The ridges of the FTLEs represent the material lines in the flow field that are the most kinematically active.[34] Specifically, LCSs explain the attracting, repelling, and shearing behavior of material lines over time and is a useful tool for describing complex flow dynamics.

To compute the finite-time Lyapunov exponent field, we consider an arbitrary two-dimensional velocity field on a domain D and a time interval $I = [t_0, t_0 + T]$. Fixing the initial time, t_0, and a desired finite time, T, a flow map advects a particle starting at time t_0 from its initial position r_0 to its corresponding position at the final time $t_0 + T$. The flow map, $\Phi_{t_0}^t$, is given as

$$\Phi_{t_0}^t : r_0 \mapsto r(r_0, t_0, t) = r_0 + \int_{t_0}^t u(r(\tau), \tau)\, d\tau, \tag{1}$$

where $u(r, t)$ is the fluid velocity field and $r(t)$ is the particle trajectory.[2] The FTLE is then given as

$$\sigma(r_0, t_0 + T, T) = \frac{1}{|T|} \ln \sqrt{\lambda_{\max}(\Delta)}, \tag{2}$$

where

$$\Delta(r_0, t_0 + T, T) = \left(\frac{d\phi_{t_0}^{t_0+T}(r_0)}{dr_0}\right)^* \left(\frac{d\phi_{t_0}^{t_0+T}(r_0)}{dr_0}\right)$$

is the right Cauchy–Green deformation tensor, * denotes the adjoint, and $\lambda_{\max}(\Delta)$ is the associated maximum eigenvalue of Δ.

We compute FTLE values at every point in the domain to obtain the FTLE field for the flow for a chosen finite time. Areas in which nearby particles separate exponentially over time will have high FTLE values, while regions where nearby particles stay close together will yield low FTLE values. Ridges of high FTLE values will correspond to LCSs.[2]

B. Maxey–Riley equation

The dynamics of inertial particles are different to that of passive tracer particles in a fluid flow as the motion of inertial particles can depict behavior such as clustering and dispersion.[35] As discussed in the Introduction, preferential aggregation of inertial particles can be seen in a range of phenomena in ocean and atmospheric transport. Our objective in this work is to explore the preferential aggregation of inertial particles and their corresponding iFTLE field in various flows for different values of Stokes number and density ratios.

To obtain the FTLE field for inertial particles (iFTLEs), we use the Maxey–Riley (MR) equation,[36] given as

$$\begin{aligned} m_p \dot{v} = m_f \frac{D}{Dt} u(r(t), t) - \frac{1}{2} m_f \frac{d}{dt}\left[v - u(r(t), t) - \frac{1}{10} a^2 \nabla^2 u(r(t), t)\right] \\ - 6\pi a\mu X(t) + \left(m_p - m_f\right) g - 6\pi a^2 \mu \int_0^t d\tau \frac{\frac{dX(\tau)}{d\tau}}{\sqrt{\pi\nu(t-\tau)}}, \end{aligned} \tag{3}$$

with

$$X(t) = v(t) - u(r(t), t) - \frac{1}{6} a^2 \nabla^2 u,$$

and where the overdot denotes $\frac{d}{dt}$ and $\nabla^2 = \frac{\partial^2}{\partial x^2} + \frac{\partial^2}{\partial y^2}$.

Equation (3) is valid for two-dimensional (2D) or three-dimensional (3D) flows, where $r(t)$ denotes the position of a spherical particle at time t, $v(t) = \dot{r}(t)$ is the corresponding velocity of the particle, m_p is the mass of the inertial particle, m_f is the mass of the fluid displaced by the particle, $u(r(t), t)$ is the velocity of the fluid at the location $r(t)$ and time t, μ is the viscosity of the underlying fluid, a is the radius of the particle, and g is the acceleration due to gravity. In Eq. (3), the derivative $D\,u/D\,t$ is the material derivative, and $d/d\,t$ is the usual total derivative. The material derivative, given by

$$\frac{Du}{Dt} = \frac{\partial u}{\partial t} + (u \cdot \nabla) u = \frac{\partial u}{\partial t} + u_x \frac{\partial u}{\partial x} + u_y \frac{\partial u}{\partial y}, \tag{4}$$

is the hydrodynamical derivative taken along the path of a fluid element, whereas the total derivative

$$\frac{du}{dt} = \frac{\partial u}{\partial t} + (v \cdot \nabla) u = \frac{\partial u}{\partial t} + \frac{\partial u}{\partial x}\frac{dx}{dt} + \frac{\partial u}{\partial y}\frac{dy}{dt} \tag{5}$$

is taken along the particle's trajectory.[37] The $a^2\nabla^2 u$ term is the Faxén correction term, and the integral term on the right-hand side of Eq. (3) is the Basset–Boussinesq history term. If the time scale for a particle to revisit a region it has visited earlier is large in comparison to the viscous diffusion time scale, then the magnitude of the history force is much smaller than the magnitude of the Stokes drag. To leading order, the integral term scales out of the dominant balance .[38] Removing the Basset–Boussinesq term from Eq. (3) leads to a simplified form of the Maxey–Riley equation, given as

$$\begin{aligned} m_p \dot{v} = m_f \frac{D}{Dt} u(r(t), t) - \frac{1}{2} m_f \frac{d}{dt}\left[v - u(r(t), t) - \frac{1}{10} a^2 \nabla^2 u(r(t), t)\right] \\ - 6\pi a\mu\left[v(t) - u(r(t), t) - \frac{1}{6} a^2 \nabla^2 u\right] + \left(m_p - m_f\right) g. \end{aligned} \tag{6}$$

We non-dimensionalize (details are provided in Appendix A) the MR equation given by Eq. (6) using the velocity scale, U, and the length scale, L, of the external flow. Introducing the non-dimensional variables $\hat{r}$, $\hat{u}$, and $\hat{t}$ so that $r \to \hat{r}L$, $u \to \hat{u}U$, and $t = \frac{L}{U}\hat{t}$, one obtains the non-dimensional MR equation, including buoyancy and the Faxén correction, as

$$\begin{aligned} \hat{r}''(t) = R\frac{D}{D\hat{t}}\hat{u}(r(\hat{t}), \hat{t}) + \frac{1}{2} R \frac{d}{d\hat{t}}\hat{u}(r(\hat{t}), \hat{t}) + \frac{1}{St}\left[\hat{u}(r(\hat{t}), \hat{t}) - \hat{r}'(\hat{t})\right] \\ + Wn + \frac{1}{20} P^2 R \frac{d(\hat{\nabla}^2 \hat{u})}{d\hat{t}} + \frac{1}{6}\frac{P^2}{St}\hat{\nabla}^2 \hat{u}, \end{aligned} \tag{7}$$

where

$$\begin{aligned} St^{-1} &= \frac{6\pi a\mu L}{\left(m_p + \frac{1}{2}m_f\right) U}, \quad R = \frac{m_f}{m_p + \frac{1}{2}m_f}, \\ W &= \frac{m_p - m_f}{6\pi a\mu U St} g, \quad \text{and} \quad P = \frac{a}{L}, \end{aligned} \tag{8}$$

and where $\dot{r} = U\hat{r}'$, $\ddot{r} = \frac{U^2}{L}\hat{r}''$, with $'$ denoting $d/d\hat{t}$. In Eq. (7), St is the Stokes number, defined as the ratio of the characteristic time of a particle to a characteristic time of the flow, R is the density ratio parameter, P is the ratio of the radius of particle size to the characteristic length of the flow, and n is the unit vector pointing in the direction of gravity.[39] If $R = 2/3$, the particles have the same density as that of the carrier fluid, and we refer to those particles as neutrally buoyant. If $R > 2/3$, then the particles are lighter than the carrier fluid, and we refer to them as bubbles. Similarly, particles with $R < 2/3$ are denser than the carrier fluid, and we refer to them as aerosols.[39]

For the sake of simplicity, we ignore buoyancy effects, and the non-dimensional MR equation with Faxén correction has a final form given by

$$\hat{r}''(t) = R\frac{D}{D\hat{t}}\hat{u}(r(\hat{t}),\hat{t}) + \frac{1}{2}R\frac{d}{d\hat{t}}\hat{u}(r(\hat{t}),\hat{t}) + \frac{1}{St}[\hat{u}(r(\hat{t}),\hat{t}) - \hat{r}'(\hat{t})] + \frac{1}{20}P^2R\frac{d(\hat{\nabla}^2\hat{u})}{d\hat{t}} + \frac{1}{6}\frac{P^2}{St}\hat{\nabla}^2\hat{u}. \tag{9}$$

If the Faxén correction term, used to justify nonuniform flow effects encountered by the inertial particle, is ignored, Eq. (9) simplifies to

$$\hat{r}''(t) = R\frac{D}{D\hat{t}}\hat{u}(r(\hat{t}),\hat{t}) + \frac{1}{2}R\frac{d}{d\hat{t}}\hat{u}(r(\hat{t}),\hat{t}) + \frac{1}{St}[\hat{u}(r(\hat{t}),\hat{t}) - \hat{r}'(\hat{t})]. \tag{10}$$

It is often assumed that for sufficiently small particles, the total derivative d/dt is equal to the material derivative D/Dt. In that case, Eq. (10) reduces further to

$$\hat{r}''(t) = \frac{3}{2}R\frac{d}{d\hat{t}}\hat{u}(r(\hat{t}),\hat{t}) + \frac{1}{St}[\hat{u}(r(\hat{t}),\hat{t}) - \hat{r}'(\hat{t})]. \tag{11}$$

Equation (11) and similar forms of the MR equation are often used in the literature.[37,39–42] In our work, we will consider Eqs. (9)–(11) to understand how the iFTLEs and particle aggregation are affected by the Faxén correction and the assumption that the material derivative equals the total derivative. In Secs. III C 1–III C 2, we present an analysis of the double-gyre flow to set a benchmark for comparison. We then extend the analysis to the Bickley jet and eddy-quadrupole flows and finally consider ocean surface velocity data from Monterey Bay, California. In all cases, we explore the preferential aggregation of inertial particles and their iFTLE fields.

III. DOUBLE-GYRE FLOW

The double-gyre (DG) flow is a simple and very well-studied fluid model consisting of two counter-rotating vortices where the separatrix between the gyres oscillates periodically to emulate wind forcing. The double-gyre flow is characterized by the stream function,[2,33]

$$\psi(x,y,t) = A\sin(\pi f(x,t))\sin(\pi y), \tag{12}$$

where

$$\begin{aligned} f(x,t) &= a(t)x^2 + b(t)x, \\ a(t) &= \varepsilon\sin(\omega t), \\ b(t) &= 1 - 2\varepsilon\sin(\omega t), \end{aligned} \tag{13}$$

and where $\frac{\omega}{2\pi}$ is the frequency of the separatrix oscillation, A is the approximate amplitude of the velocity vectors, and ε determines the amplitude of the left-right motion of the separatrix between the two gyres. When $\varepsilon = 0$, the flow becomes time-independent, and if $\varepsilon \neq 0$, the gyres undergo a periodic expansion and contraction in the x direction.[2]

Taking derivatives of the streamfunction, the velocity field for the double-gyre model is found to be

$$\begin{aligned} \dot{x} &= -\frac{\partial\psi}{\partial y} = -\pi A\sin(\pi f(x,t))\cos(\pi y), \\ \dot{y} &= \frac{\partial\psi}{\partial x} = \pi A\cos(\pi f(x,t))\sin(\pi y)\frac{\partial f}{\partial x}. \end{aligned} \tag{14}$$

Unless otherwise stated, the parameter values for the time-dependent DG flow used throughout this work are $A = 0.1$, $\omega = 6\pi/10$, and $\varepsilon = 0.25$.

A. Non-inertial FTLE field

The FTLE field is computed to identify the coherent structures associated with the double-gyre flow. We initialized 500×250 passive tracer particles uniformly on a rectangular $[0, 2] \times [0, 1]$ grid. Using a fourth-order Runge–Kutta method with a time integration step size of 0.01, we calculated the non-inertial particle trajectories by advecting the particles according to the velocity field given by Eq. (14). If a particle exits the flow field, the FTLE field is computed based on the particle's position on the boundary. The FTLE fields are calculated using Eq. (2) and the method described in Sec. II A.

Figure 1 shows the FTLE field for the time-independent ($\varepsilon = 0$) and time-dependent case for finite times of $T = 15$. For the time-independent case, one can see a ridge associated with maximal FTLE values, which forms a transport barrier between the two gyres. This

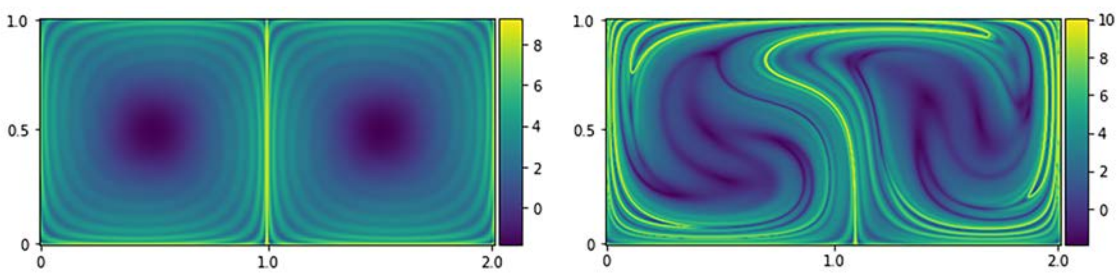

FIG. 1. Forward-time FTLE field for (left) the time-independent, and (right) the time-dependent double-gyre flow at initial time $t_0 = 0$ for $T = 15$. The parameter values used in the computation are $A = 0.1$, $\omega = 6\pi/10$, and (left) $\varepsilon = 0$ and (right) $\varepsilon = 0.25$.

ridge corresponds to the separatrix. Consideration of the FTLE field in Fig. 1 shows that the FTLE field remains constant in time, which clearly makes sense since, in the time-independent case, the velocity field is not changing in time. Finer structures will be illuminated as the finite integration time is increased.

However, for the time-dependent case, when the flow is changing in time, the FTLE field evolves in time (Fig. 1 shows a snapshot at initial time $t_0 = 0$). Beyond their time-dependent nature, the LCSs, denoted by the ridges of maximal FTLE values, are much more complicated than the time-independent LCSs, and they cannot be seen by simply observing the velocity field. As with the time-independent LCSs, an increase in the finite time of integration results in finer, higher density, LCSs.

B. Inertial FTLE (iFTLE) field

The iFTLE field is computed to identify the LCSs associated with the double-gyre flow. We initialized 500 × 250 inertial particles uniformly on a rectangular [0, 2] × [0, 1] grid. Using a fourth-order Runge–Kutta method with a time integration step size of 0.01, we calculated the inertial particle trajectories by advecting the particles using Eq. (11). As with non-inertial particles, if an inertial particle exits the flow field, the iFTLE field is computed based on the particle's position on the boundary. The iFTLE fields are calculated using Eq. (2) and the method described in Sec. II A.

The forward-time iFTLE fields at $T = 15$ are shown in Fig. 2. For aerosols ($R = 0$), the iFTLE field looks similar to non-inertial particles up to $St = 0.2$. For $St = 0.5$, we see that there is a significant difference in the iFTLE field, and the particles will cluster along a structure, which runs between the two gyres (details of the particle aggregation are provided in Sec. III C). For bubbles ($R = 1$), one can see low FTLE values in the center of the gyres. This is consistent with particle aggregation inside each of the gyres as explored in Sec. III C.

C. Preferential aggregation of particles

To understand the dynamics of inertial particles in a DG flow model, we explore the preferential aggregation of inertial particles and the iFTLE fields for various Stokes numbers and density ratios using Eq. (11). Figure 3 (Multimedia available online) compares the particle aggregation of aerosols, neutrally buoyant particles, and bubbles at time $t = 15$ after advecting the inertial particles using the MR equation given by Eq. (11) for varying Stokes number. We see that aerosols ($R = 0$) aggregate toward the maximal iFTLE ridges while bubbles ($R = 1$) are repelled from the maximal iFTLE ridges, forming clusters in the center of the gyres instead. Neutrally buoyant particles ($R = 2/3$) follow the underlying flow without preferential clustering. This behavior is consistent with the findings of Sudharsan *et al.*,[39] who first studied particle aggregation in a double-gyre flow. In Secs. III C 1–III C 5, we examine the aerosol and bubble cases separately and study how their aggregation depends on the Stokes number.

1. Aerosol aggregation

We examine the preferential aggregation of aerosols ($R = 0$) for three choices of the Stokes number. Figure 4 shows the aerosol distribution at $t = 15$ for $St = 0.1$, $St = 0.2$, and $St = 0.5$. Across this range, aerosols aggregate along the maximal iFTLE ridges. As the Stokes number increases, the clustering becomes more pronounced as aerosols aggregate more rapidly toward the LCSs.

2. Bubble aggregation

We similarly examine the preferential aggregation of bubbles ($R = 1$) for the same three choices of the Stokes number. Figure 5 shows the aggregation of bubbles at $t = 15$ for $St = 0.1$, $St = 0.2$, and $St = 0.5$. Unlike aerosols, bubbles are repelled from the maximal iFTLE ridges and instead cluster in the centers of the two gyres. Like

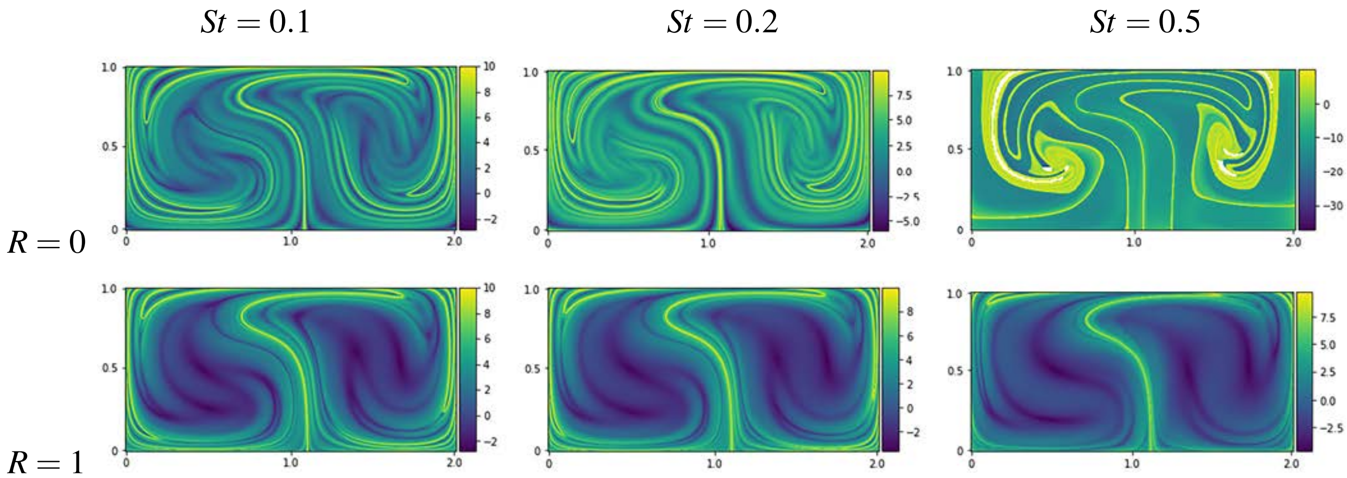

FIG. 2. Forward-time iFTLE field at initial time $t_0 = 0$ with $T = 15$ for (top) aerosols ($R = 0$), and (bottom) bubbles ($R = 1$), for Stokes numbers (left) $St = 0.1$, (middle) $St = 0.2$, and (right) $St = 0.5$.

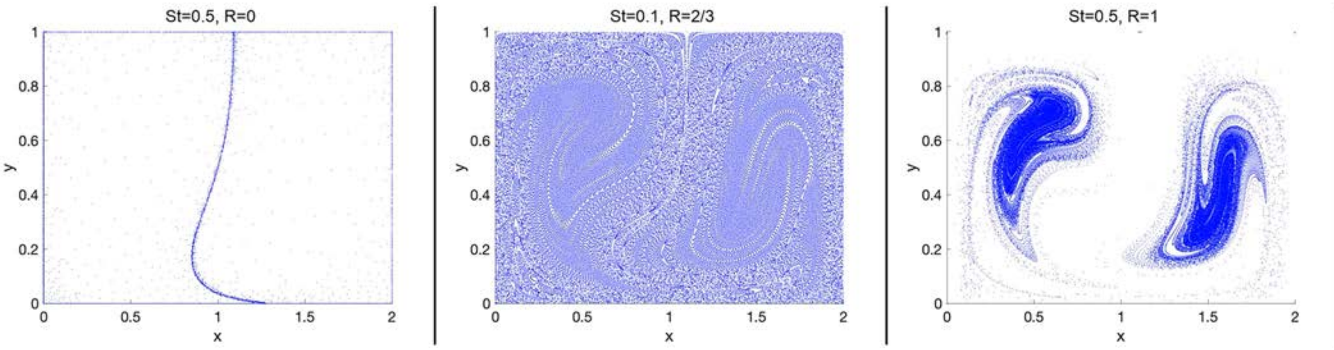

FIG. 3. Preferential aggregation for inertial particles at $t = 15$ for (left) aerosols ($R = 0$, $St = 0.5$), (middle) neutrally buoyant ($R = 2/3$, $St = 0.1$), and (right) bubbles ($R = 1$, $St = 0.5$). Multimedia available online.

aerosols, as the Stokes number increases, bubbles aggregate more rapidly and tightly toward the center of the gyres.

To further illustrate the dynamics of inertial particles, we examined the particle aggregation on a density ratio spectrum for a fixed Stokes number. Figure 20 in Appendix B shows the particle aggregation of aerosols, neutrally buoyant particles, and bubbles at time $t = 15$ after advecting the inertial particles using the MR equation given by Eq. (11) for $St = 0.5$. Starting with aerosols, the inertial particles are clustered tightly along the maximal iFTLE ridges. As R increases, particles gradually become less clustered and will be spread throughout the domain when they are neutrally buoyant ($R = 2/3$). As R increases further, particles will cluster in the center of the gyres.

Backward-time FTLEs can be used to identify the attracting LCSs and are, therefore, often used to identify structures where particle clustering occurs. However, in this work, we are dealing with two different classes of inertial particles, namely, heavy aerosols that accumulate on attracting structures and light bubbles that move away from the attracting structures into vortex cores. Because of the two-sided nature of the dynamics, we have used the forward-time FTLE specifically because its ridges delineate the repelling structures, which act as the critical transport barriers that dynamically separate the regions of phase space in which the different types of inertial particles are funneled into.

3. Faxén correction

As previously discussed in Sec. II B, the Faxén correction terms are typically ignored for small particle sizes. To study the effect of particle size in a double-gyre flow, we examine the iFTLE fields for aerosols and bubbles by including the Faxén correction terms in our computation. Initializing 500×250 inertial particles uniformly on our domain, and using a fourth-order Runge–Kutta method with a time integration step size of 0.01, the inertial particle trajectories are computed by integrating the MR equation given by Eq. (9) with non-dimensional particle size parameter given by $P = \frac{a}{L}$.

The Maxey–Riley equation is valid for

$$St = \frac{2}{9}\left(\frac{a}{L}\right)^2 Re \ll 1, \tag{15}$$

where Re denotes the Reynolds number of the underlying fluid flow. This condition does not require Re itself to be small. Instead, the

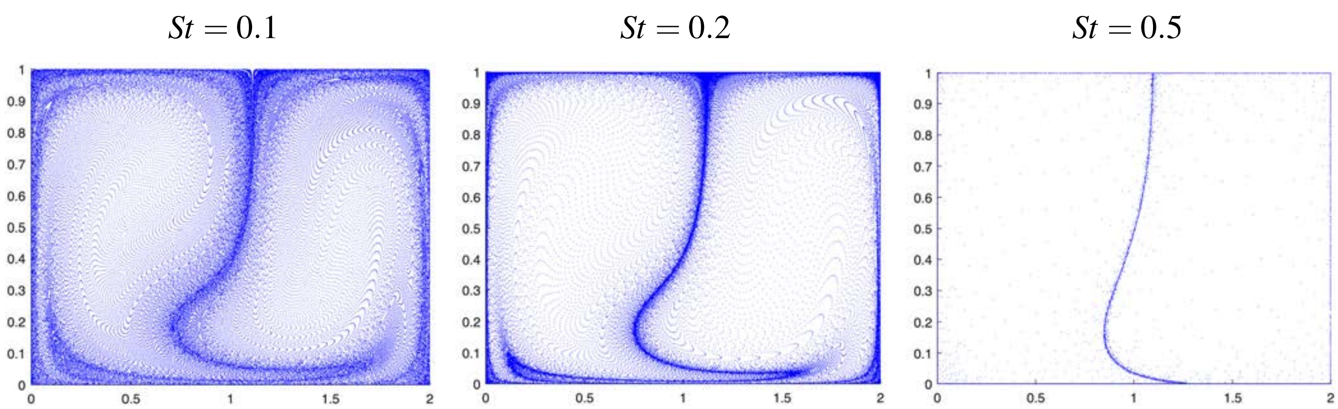

FIG. 4. Preferential aggregation of aerosols ($R = 0$) at $t = 15$ for (left) $St = 0.1$, (middle) $St = 0.2$, and (right) $St = 0.5$ in a DG flow.

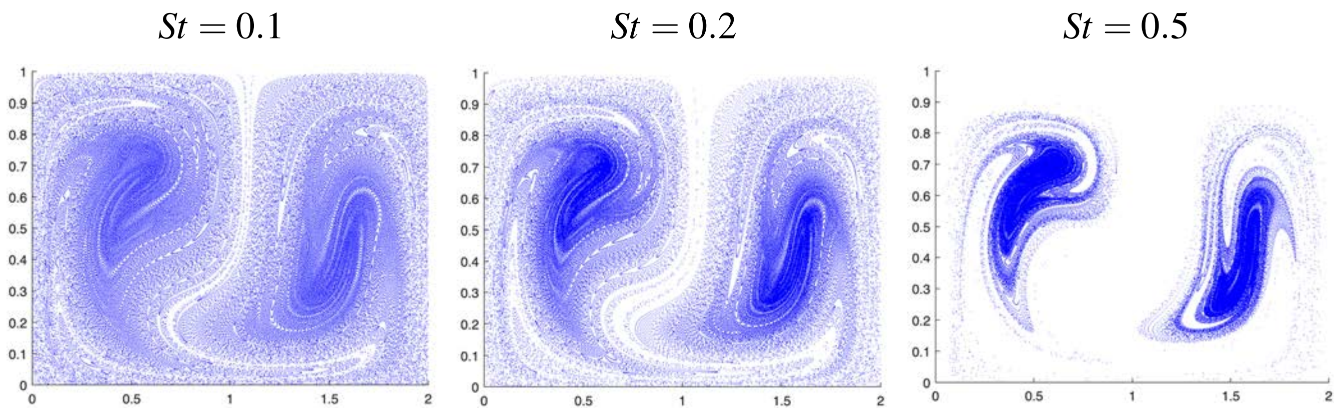

FIG. 5. Preferential aggregation of bubbles ($R = 1$) at $t = 15$ for (left) $St = 0.1$, (middle) $St = 0.2$, and (right) $St = 0.5$ in a DG flow.

particle Reynolds number Re_p, where the particle diameter is the characteristic length scale, and the slip velocity of the particle relative to the fluid velocity is the characteristic velocity scale, must be small.[37,38] The small particle sizes and slip velocities used throughout this work keep Re_p small even when the background flow has a high Reynolds number.

We have considered a wide range of P values ranging from $P = 10^{-6}$ to $P = 1$. Figure 6 shows the forward-time iFTLEs for aerosols and bubbles for $P = 1$ and for two choices of Stokes number, which satisfy Eq. (15) for this choice of P. For aerosols ($R = 0$), the iFTLE fields look similar to the iFTLE fields found using the MR equation without the Faxén correction. With the inclusion of the Faxén correction, particles will aggregate more slowly toward the LCS. For bubbles ($R = 1$), the iFTLE fields again look similar to the iFTLE fields found using the MR equation without the Faxén correction, with the exception that stronger FTLE ridges are seen around the boundary of the gyres. There is no significant difference in the coherent structures between the two choices of Stokes number. The results do not appreciably change for our range of P values from $P = 10^{-6}$ to $P = 1$. Overall, the Faxén correction provides a negligible contribution to the iFTLE structure for small particles in flows without high shear gradients. Thus, the simplified version of the MR equation without the Faxén correction terms is sufficient to capture the inertial particle dynamics across the DG flow.

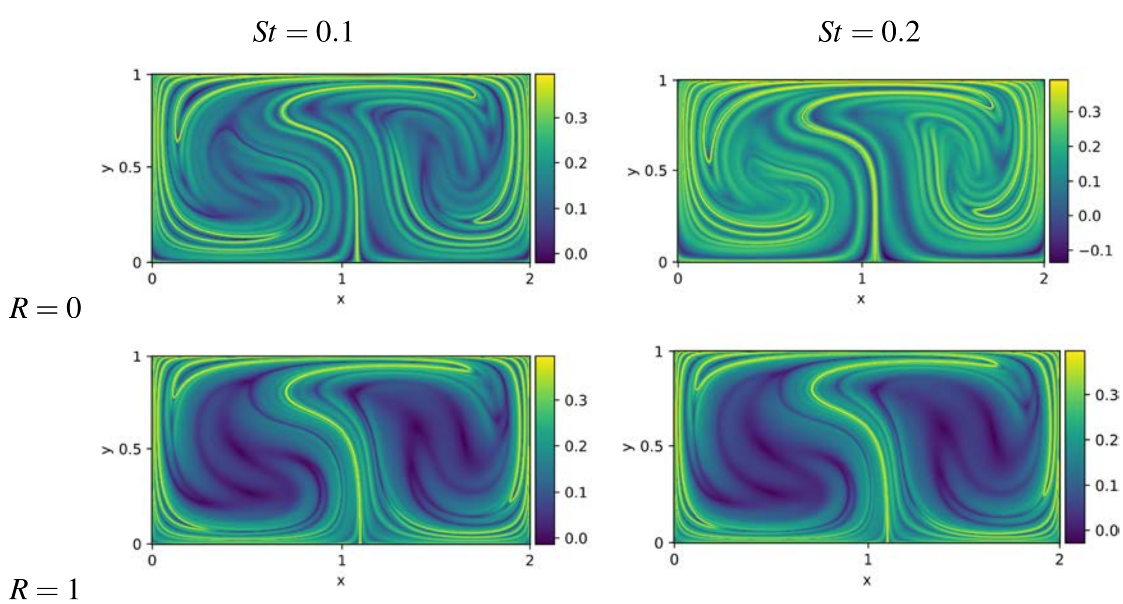

FIG. 6. Forward-time iFTLE field computed with the MR equation including Faxén correction terms at the initial time $t_0 = 0$ with $T = 15$ for (top) aerosols, and for (bottom) bubbles, for a Stokes number of (left) $St = 0.1$, and (right) $St = 0.2$, and with $P = 1$. The parameter values used in the computation are $A = 0.1$, $\omega = 6\pi/10$, and $\varepsilon = 0.25$.

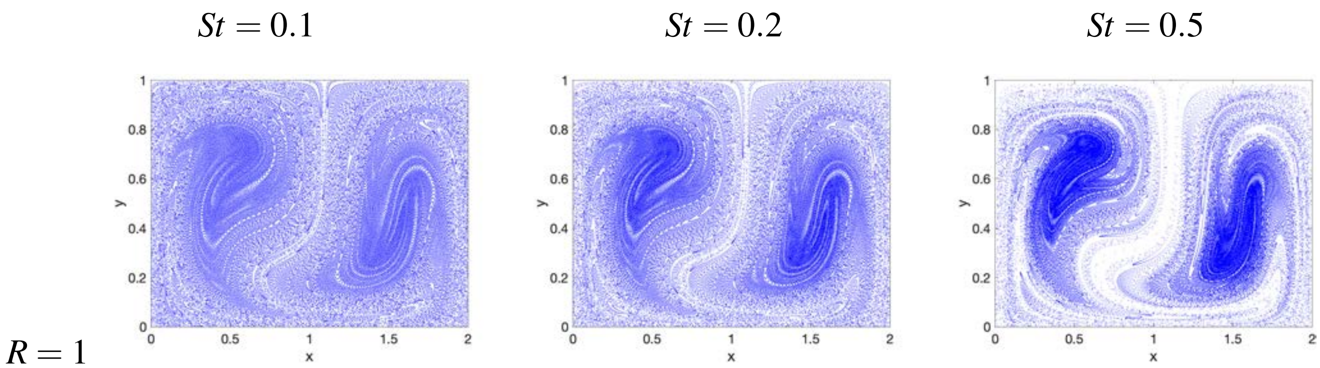

FIG. 7. Preferential aggregation for bubbles ($R = 1$) at $t = 15$ for the scenario where the total derivative is not assumed to be equal to the material derivative. The computations are performed for a Stokes number of (left) $St = 0.1$, (middle) $St = 0.2$, and (right) $St = 0.5$. The parameter values used in the computation are $A = 0.1$, $\omega = 6\pi/10$, and $\varepsilon = 0.25$.

4. Material derivative vs total derivative

As mentioned previously, it is often assumed that for sufficiently small particle size, the total derivative and the material derivative are the same. However, in general, it is not necessarily the case that the material derivative and total derivative are identical. Therefore, we have examined the preferential aggregation for inertial particles using Eq. (10), which does not assume the two derivatives are equal.

For aerosols with $R = 0$, the particle trajectory does not depend on the fluid acceleration as the first term on the right-hand side of Eq. (11) evaluates to 0. Thus, there will be no effect due to the difference between the total derivative and the material derivative. Figure 7 shows the particle aggregation of bubbles ($R = 1$) at $t = 15$ when the total derivative and the material derivative are not assumed to be identical. One can notice that even though the preferential aggregation is similar in that the particles are accruing in the gyre centers, the aggregation is occurring more slowly when the two derivatives are not assumed to be equal. Overall, the assumption that the material derivative equals the total derivative preserves the qualitative attractor structure, changing only the timescale of aggregation of inertial particles onto their attractors.

5. Preferential aggregation of particles with the inclusion of Coriolis force

The Coriolis force is an inertial force that acts on objects that are moving within a rotating frame of reference, such as the Earth. To model the dynamics of inertial particles in actual geophysical flows, such as oceanic flows, we add a Coriolis force term into the Maxey–Riley equation to account for the effect of the Earth's rotation. We start with the simplest form of the Maxey–Riley equation given by Eq. (11) and add the Coriolis force as

$$\ddot{r}(t) = \frac{3}{2}R\left(\frac{D}{Dt}u(r(t),t) + \underline{2\vec{\Omega} \times u(r(t),t)}\right) + \frac{1}{\mathrm{St}}[u(r(t),t) - \dot{r}(t)]\underline{-2\vec{\Omega} \times \dot{r}(t)}, \tag{16}$$

where the underlined terms are the Coriolis force, and where $\vec{\Omega}$, the rotation vector, is given at a latitude φ so that

$$\vec{\Omega} = (\Omega_x, \Omega_y, \Omega_z) = (0, \Omega\cos\varphi, \Omega\sin\varphi). \tag{17}$$

In Eq. (17), the components of $\vec{\Omega}$ are defined so that in the local coordinate system, the x-direction runs east-west, the y-direction runs north-south, and the z-direction is vertically perpendicular to the surface, and the scalar $\Omega = \frac{2\pi}{24\,\mathrm{hrs}} \approx 7.29 \times 10^{-5}\,\mathrm{s}^{-1}$ is the magnitude of the Earth's angular velocity vector. The Coriolis force has a form given by

$$2\vec{\Omega} \times \dot{r}(t) = 2\Omega \cdot (0, \cos\varphi, \sin\varphi) \times \vec{v}. \tag{18}$$

Usually, $\cos\varphi$ is neglected as the vertical component is typically small compared to gravity, and one assumes that

$$2\Omega\sin\varphi = f. \tag{19}$$

The terms associated with the Coriolis force can now be written as

$$2\vec{\Omega} \times \vec{v} = (0, 0, f) \times (v_x, v_y, v_z) = (-fv_y, fv_x, 0), \tag{20}$$

and, using the same argument,

$$2\vec{\Omega} \times \vec{u} = (-fu_y, fu_x, 0). \tag{21}$$

We note that while the Coriolis force is added to the MR equation, the underlying DG velocity field remains unchanged. This approach is physically consistent given that the DG flow, as well as the Bickley jet and eddy-quadrupole flow examined in Sec. IV, are strictly kinematic models that do not solve the Navier–Stokes equations. However, for flows that are solutions to the Navier–Stokes equations in a rotating frame, geostrophic balance, where the Coriolis force balances the pressure gradient, is the leading-order balance in the horizontal direction. Large-scale ocean circulations are usually modeled via the β-plane approximation and Sverdrup balance as described by quasi-geostrophic theory (e.g., Pedlosky[43]), and analogous rotational dynamics govern simpler setups like Kolmogorov flow. Since we utilize the kinematic flow models as a benchmark to isolate and study the effect of rotation on inertial particle dynamics, we intentionally keep the base flow fixed. Crucially, however, for the application of our framework to ocean data in Sec. V, the velocity field inherently captures all such dynamic rotational effects and physical balances.

To explore the preferential aggregation of inertial particles in a double-gyre flow with the inclusion of Coriolis force, we initialized 500×250 inertial particles on a uniform grid, and the fluid particles were advected using the Maxey–Riley equation given by Eq. (16). As demonstrated numerically by Provenzale,[44] the presence of the Coriolis force pushes heavy impurities out of cyclonic vortices and pushes them toward the center of anticyclonic vortices. Moreover, Beron-Vera *et al.*[45] and Haller *et al.*[46] showed theoretically that in a cyclonic rotationally coherent vortex [anticlockwise in the Northern Hemisphere (NH), clockwise in the Southern Hemisphere (SH)], there exists a finite-time repeller for heavy particles and a finite-time attractor for light particles that stays close to the vortex center. By contrast, in an anticyclonic rotationally coherent vortex (clockwise in the NH, anticlockwise in the SH), there exists a finite-time attractor for heavy particles and a finite-time repeller for light particles that stays close to the vortex center.[46] We have computationally verified these theoretical statements for the double-gyre flow as described below. Since the Maxey–Riley equation is in non-dimensional form, we must multiply the dimensional scalar Ω by a time scale so that the Coriolis force is also non-dimensional. We have chosen to use time scales of 5000 and 10 000 s for aerosols, and time scales of 8000 and 15 000 s for bubbles for two different Stokes numbers in order to highlight the behavior of heavy and light particles in a rotationally coherent vortex. We note that the timescales used here to make the Coriolis force non-dimensional are independent of the non-dimensionalization described in Appendix A, which uses the flow's intrinsic scales U and L. Since Earth's angular velocity Ω is fixed, varying the timescale T is equivalent to varying the effective Rossby number $Ro = \frac{U}{fL}$ of the system. The choice of T, thus, determines the ratio of inertial forces to Coriolis force, which allows us to explore the strength of rotation in the aggregation of inertial particles.

Figure 8 shows that in the NH (cyclonic rotational frame), the heavy, aerosol particles are pushed out of the right cyclonic gyre toward the center of the left anti-cyclonic gyre, and in the SH (anti-cyclonic rotational frame), the heavy, aerosol particles are pushed out of the left anti-cyclonic gyre toward the center of the right cyclonic gyre. The figure also shows that the fluid particles aggregate more rapidly as the strength of rotation increases and for a higher Stokes number. Similarly, the light bubbles are pushed out of the left anti-cyclonic gyre toward the center of the right cyclonic gyre in the NH (cyclonic rotational frame), while the light bubbles are pushed out of the right cyclonic gyre toward the center of the left anti-cyclonic gyre in the SH (anti-cyclonic rotational frame). Similar to aerosols, the fluid particles aggregate more rapidly as the strength of rotation increases and higher Stokes number. Figure 21 in Appendix B shows the preferential aggregation of aerosols and bubbles in a DG flow with the inclusion of the Coriolis force at additional values of the strength of rotation.

Overall, our results show that with the inclusion of the Coriolis force, aerosols are expelled from cyclonic gyres into anticyclonic gyres, and bubbles are expelled from anticyclonic gyres into cyclonic gyres in the cyclonic rotational frame. The behavior of both aerosols and bubbles is reversed in the anticyclonic rotational frame. The rate of aggregation of inertial particles onto these attractors increases with the strength of rotation.

IV. EXTENSION TO OTHER GEOPHYSICAL FLOWS

Building on the double-gyre benchmark, we now present the dynamics of inertial and non-inertial particles in two additional kinematic models: the Bickley jet, which represents a zonal jet flanked by counter-rotating vortices, and the eddy-quadrupole flow, which represents a multi-eddy configuration of the kind found in eddy-rich ocean regions.

A. Bickley jet

We now consider another type of geophysical fluid-flow model, namely, a zonal flow. A zonal flow is a natural, large-scale flow that follows latitudinal lines and occurs in both the ocean and the atmosphere.[47] Some examples of zonal flows are the Gulf Stream, the polar night jet above Antarctica,[47] and the East-West winds of Jupiter, Saturn, and Neptune.[48] Specifically, we consider the Bickley jet, which is an idealized model used to study the eastward zonal jet that is flanked by counter-rotating vortices. The Bickley jet is modeled by a time-dependent Hamiltonian, which is comprised of a steady background flow superimposed with a time-dependent perturbation.[17,49]

The stream function is modeled as

$$\psi(x, y, t) = \psi_0(y) + \psi_1(x, y, t), \tag{22}$$

with

$$\psi_0(y) = -UL \tanh\left(\frac{y}{L}\right) \tag{23}$$

and

$$\psi_1(x, y, t) = UL\,\mathrm{sech}^2\left(\frac{y}{L}\right) \mathrm{Re}\left[\sum_{n=1}^{3} f_n(t) \exp\left(ik_n x\right)\right], \tag{24}$$

where $f_n(t) = \varepsilon_n \exp(-ik_n c_n t)$ and Re denotes the real part. The steady background flow is given by $\psi_0(y)$, and $\psi_1(x, y, t)$ is the time-dependent perturbation. It is often convenient to expand $\psi_1(x, y, t)$ as

$$\psi_1(x, y, t) = UL\,\mathrm{sech}^2\left(\frac{y}{L}\right)(\varepsilon_1 \cos(k_1(x - c_1 t)) + \varepsilon_2 \cos(k_2(x - c_2 t)) + \varepsilon_3 \cos(k_3(x - c_3 t))). \tag{25}$$

The velocity field for the Bickley jet model is computed as $\dot{x} = -\frac{\partial\psi}{\partial y}$ and $\dot{y} = \frac{\partial\psi}{\partial x}$. In Eqs. (22)–(24), U and L are the characteristic velocity scale and the characteristic length scale, respectively, and k_n, c_n, and ε_n represent the wave number, speed, and amplitude, respectively, of the traveling Rossby waves. In our analysis, we use the parameter values $U = 5.413\,824$ Mm day^{-1}, $L = 1.77$ Mm, $k_n = 2n/r_0$, where $r_0 = 6.371$ Mm is the mean radius of the earth, $\varepsilon_1 = 0.075$, $\varepsilon_2 = 0.4$, $\varepsilon_3 = 0.3$, $c_3 = 0.461U$, $c_2 = 0.205U$, and $c_1 = c_3 + (\sqrt{5} - 1)(k_2/k_1)(c_2 - c_3)$.[17,49,50] The parameter values are chosen to model how the stratospheric polar night jet stops the movement of ozone depleted air during the Southern hemisphere's late winter and early spring.[49]

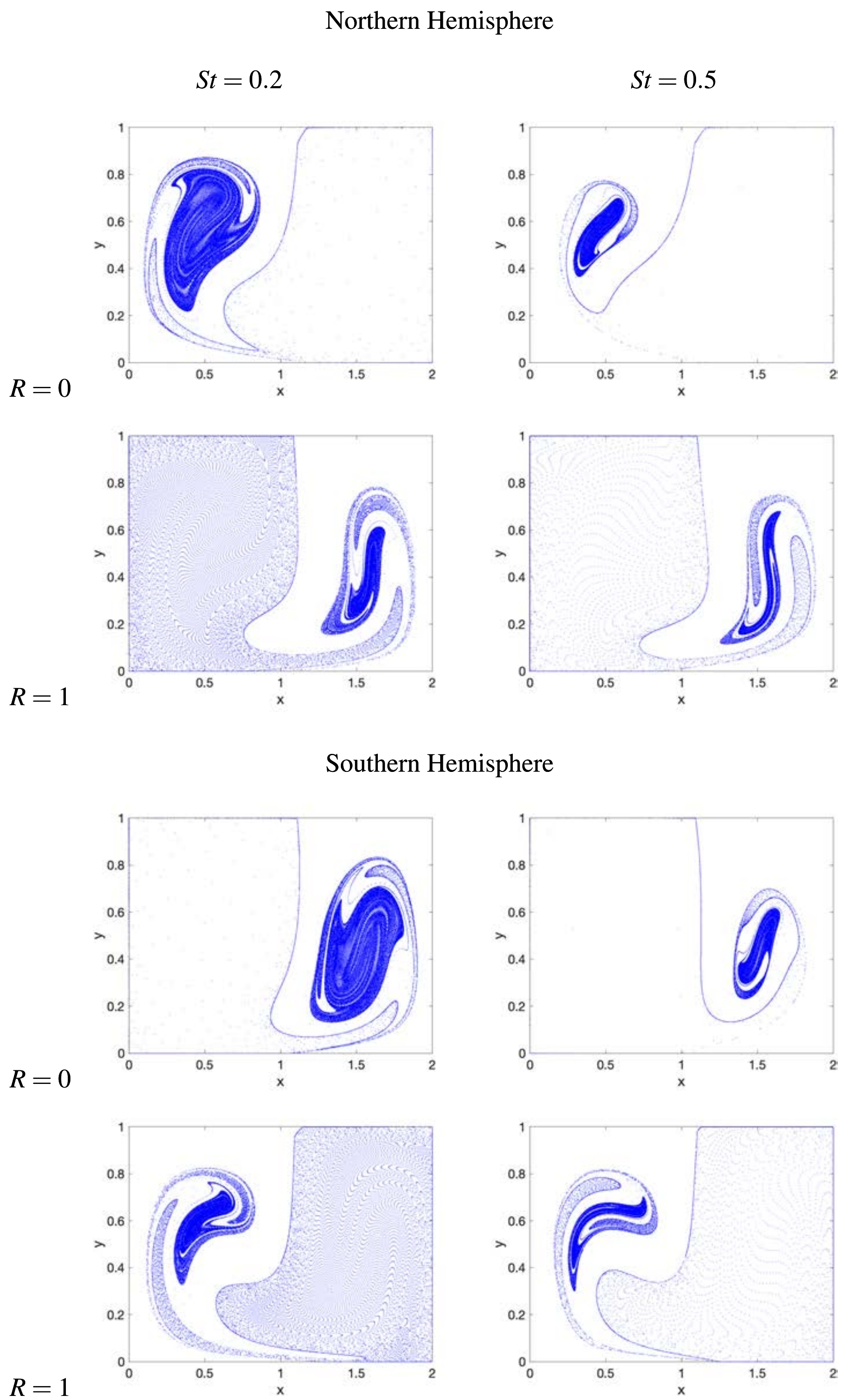

FIG. 8. Preferential aggregation of aerosols ($R = 0$, rows 1 and 3) and bubbles ($R = 1$, rows 2 and 4) at $t = 15$ in a double-gyre flow including the Coriolis force at mid-latitudes ($\varphi = \pi/4$) in the Northern Hemisphere and ($\varphi = -\pi/4$) in the Southern Hemisphere for a timescale of 10 000 s for aerosols and 15 000 s for bubbles with Stokes number (left) $St = 0.2$ and (right) $St = 0.5$.

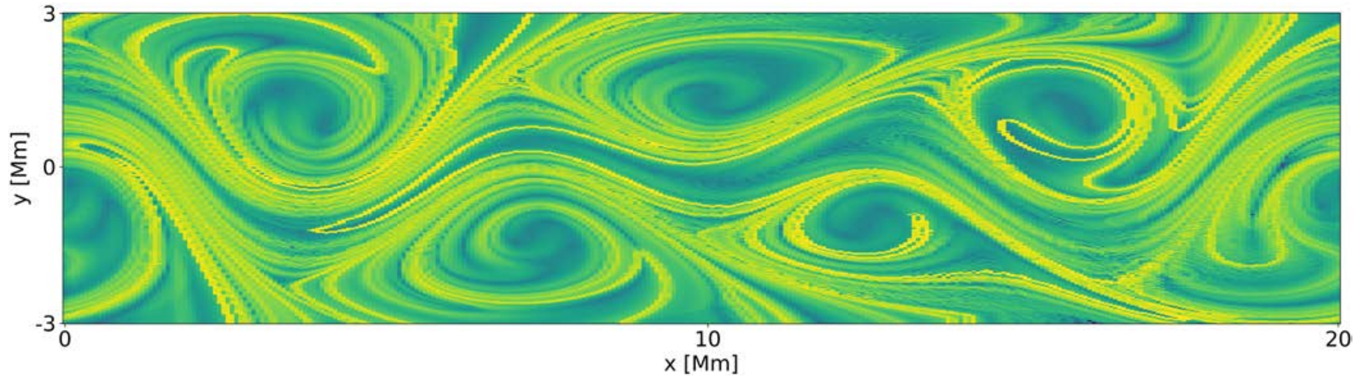

FIG. 9. Forward-time FTLE field for non-inertial particles in a Bickley jet flow at initial time $t_0 = 0$ for $T = 10$.

1. FTLE field

The FTLE field is computed to find the coherent structures associated with the Bickley jet flow field. We initialized 300 × 300 passive tracer particles uniformly on a [0, 20] × [− 3, 3] grid, and the velocity field $[\dot{x}, \dot{y}]^T$, where T denotes the transpose, was obtained by computing derivatives of the stream function using central finite differences. Using a fourth-order Runge–Kutta method with a time integration step size of 0.01, we calculated the non-inertial particle trajectories by advecting the particles according to the velocity field. Since the particles inside the strong eastward zonal jet are quickly advected out of the domain, we implemented periodic boundary conditions in the x direction. Thus, particles that leave the domain on the right-hand side of the jet, re-enter the jet on the left-hand side. The FTLE fields are calculated using Eq. (2) and the method described in Sec. II A.

Figure 9 shows the forward-time FTLE field for the Bickley jet at $T = 10$. The coherent structures seen in the figure highlight the strong eastward zonal jet, as discussed previously. Fluid particles inside the jet are swept away by the jet, while particles outside the jet can become trapped inside the vortices. Thus, the LCSs, highlighted by yellow ridges of maximal FTLEs, demarcates the separation between the jet core and the vortices. The jet core, therefore, acts as a particle transport barrier.[17] Fluid particles within the jet core stay together in the core, which leads to lower FTLE values within the core.

2. iFTLE field

To study the dynamics of inertial particles in a Bickley jet, we explore the iFTLE field computed for varying Stokes numbers and density ratios. As in the non-inertial case, 300 × 300 inertial particles are initialized uniformly on a [0, 20] × [−3, 3] grid. Using a fourth-order Runge–Kutta method with a time integration step size of 0.01, the inertial particle trajectories are computed by integrating the MR equation given by Eq. (11).

Figure 10 shows the iFTLE fields for three Stokes numbers and for aerosols ($R = 0$) and bubbles ($R = 1$) at time $T = 10$. In the case of aerosols, one can see the maximal iFTLE ridges inside the vortices with low iFTLE ridges inside the jet core. As the Stokes number increases, the density of the iFTLE ridges increases inside the vortices. For bubbles, the band of maximal iFTLE ridges around the jet core with strongly preserved vortices acts as a particle transport barrier. As the Stokes number increases, the density of maximal iFTLE ridges in the jet core gradually decreases, whereas the ridges inside the vortices become slightly more pronounced.

3. Preferential aggregation

To explore the aggregation of non-inertial and inertial particles in a Bickley jet, we consider 300 × 300 particles initialized uniformly on a [0, 20] × [− 3, 3] grid. Using a fourth-order Runge–Kutta method with a time integration step size of 0.01, the inertial particle trajectories are computed by integrating the MR equation given by Eq. (11). Figure 11 shows the preferential aggregation of aerosols ($R = 0$), neutrally buoyant particles ($R = 2/3$), and bubbles ($R = 1$) at $t = 10$ for $St = 0.2$. For aerosols, particles aggregate in the strong jet core while spreading more broadly around the vortex regions, making the vortices appear visually enlarged. For neutrally buoyant particles, the aggregation of particles, as expected, follows the underlying flow where particles spread throughout the domain in the strong jet core and counter-rotating vortices. In the limit as $St \to 0$, inertial neutrally buoyant particles will behave as non-inertial particles. In contrast, for bubbles, there is not a strong aggregation of particles in the jet core. Rather, there is more of a blending of the vortices with the core, forming a spiral-like structure. For both aerosols and bubbles, no appreciable differences are seen at lower Stokes numbers. At higher Stokes numbers ($St = 0.5$), the spiral structure of bubble aggregation becomes more pronounced, and aerosol aggregation in the jet core takes on a more complicated structure consistent with the more complicated iFTLE field shown in Fig. 10 for $St = 0.5$. The corresponding preferential aggregation results for $St = 0.5$ are shown in Fig. 22 in Appendix C.

4. Coriolis effect

To explore the preferential aggregation of inertial particles with the inclusion of the Coriolis force in the Bickley jet, we initialized 300 × 300 inertial particles on a [0, 20] × [−3, 3] grid. Using a fourth-order Runge–Kutta method with a time integration step size

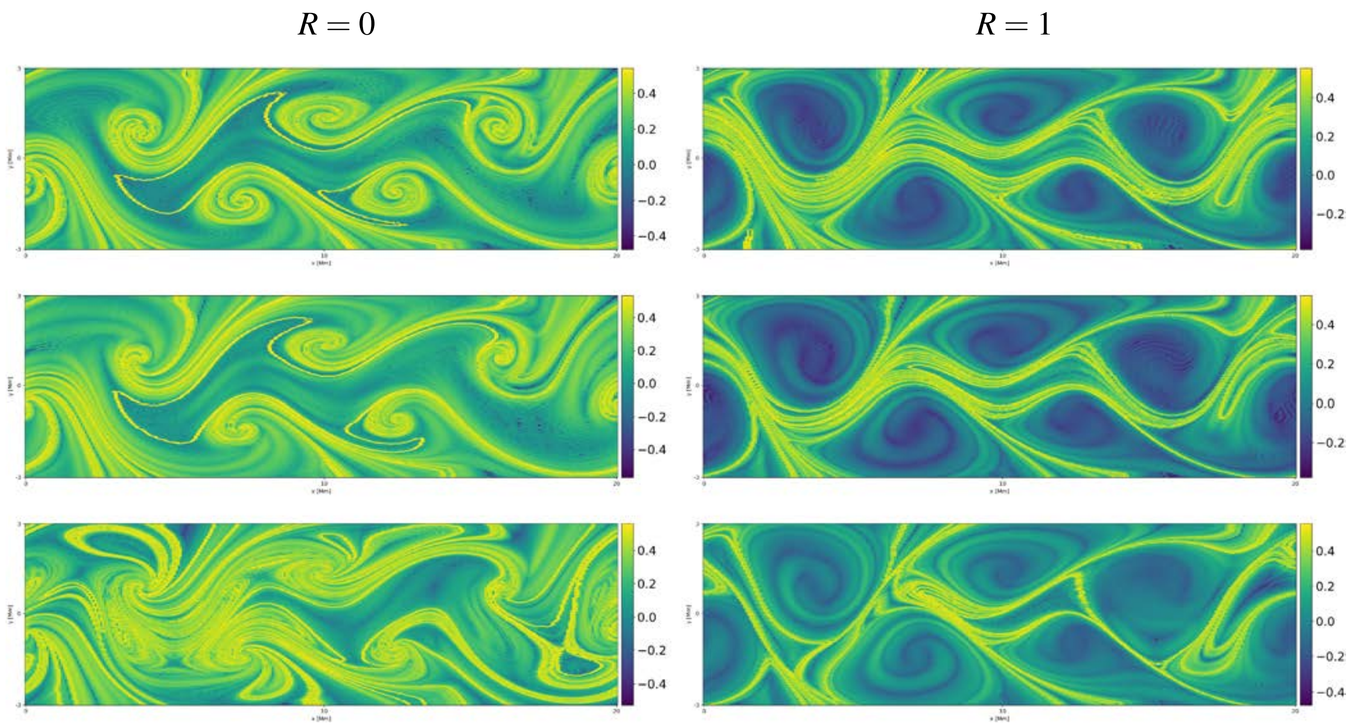

FIG. 10. Forward-time iFTLE field for inertial particles in a Bickley jet computed at initial time $t_0 = 0$ with $T = 10$ for (left column) aerosols ($R = 0$) and (right column) bubbles ($R = 1$), for Stokes numbers (top panel) $St = 0.1$, (middle panel) $St = 0.2$, and (bottom panel) $St = 0.5$.

of 0.01, the inertial particle trajectories are computed by integrating the MR equation given by Eq. (16).

Figure 12 shows the preferential aggregation of aerosols ($R = 0$) and bubbles ($R = 1$) at $t = 10$ in both hemispheres for a representative Coriolis non-dimensionalization timescale of 20 000 s and Stokes number $St = 0.1$. Although the Bickley jet parameters are tuned for the Southern Hemisphere, we show both hemispheres to demonstrate the expected hemispheric reversal. In the Southern Hemisphere, where cyclonic vortices rotate clockwise and anticyclonic vortices rotate counterclockwise, aerosols are expelled out of the vortices and jet core and aggregate along the upper flank of the separatrices bounding the vortex cores and the meandering jet, while bubbles form spiral-like structures and aggregate within the vortices along the lower boundary. In the Northern Hemisphere, where cyclonic vortices rotate counterclockwise and anticyclonic vortices rotate clockwise, the behavior is reversed: aerosols aggregate along the lower boundary and bubbles aggregate along the upper boundary. This result is consistent with the theory for heavy and light particles as explained in Sec. III C 5. The corresponding preferential aggregation results for Stokes numbers $St = 0.1$, $St = 0.2$, $St = 0.5$ and Coriolis timescales 10 000 and 20 000 s for both hemispheres are shown in Figs. 23 and 24 in Appendix C, where one can see that aerosols are increasingly swept to the boundary at higher Stokes numbers and aggregation toward the inertial attractors strengthens as the strength of rotation increases.

B. Eddy-quadrupole flow

Eddies are localized rotating structures in a fluid flow and are commonly seen in chaotic and turbulent flow regimes. Eddies are seen in both the ocean and the atmosphere, and play a key role in ocean circulation and regulating air–sea exchanges.[51] For instance, the Kuroshio extension, a western boundary current of the North Pacific Subtropical Gyre, which flows northeastward along Japan's Pacific coast before entering the North Pacific as a free jet, is characterized by strong mesoscale and submesoscale eddy activity.[52] The Southern Ocean is one of the most eddy-rich regions; eddies in this region are crucial in regulating the response of key current systems, such as the Antarctic Circumpolar Current, which control the exchange of nutrients, heat, and salt between ocean basins and significantly impact the carbon cycle and deep ocean heat content.[53] There is a positive correlation between sea surface temperature anomalies from cyclonic and anticyclonic eddies and changes in near-surface wind speed, cloud cover, cloud water content, rainfall rate, and likelihood of rain throughout the Southern Ocean.[54]

We now consider the eddy-quadrupole flow,[55] a simple analytic model that captures key features of eddy-rich ocean regions as discussed above. This eddy-quadrupole flow model is an incompressible flow in which a carefully chosen time dependence induces a symmetric transition of the flow from a four-eddy configuration to an eight-eddy configuration.[55] The streamfunction of the

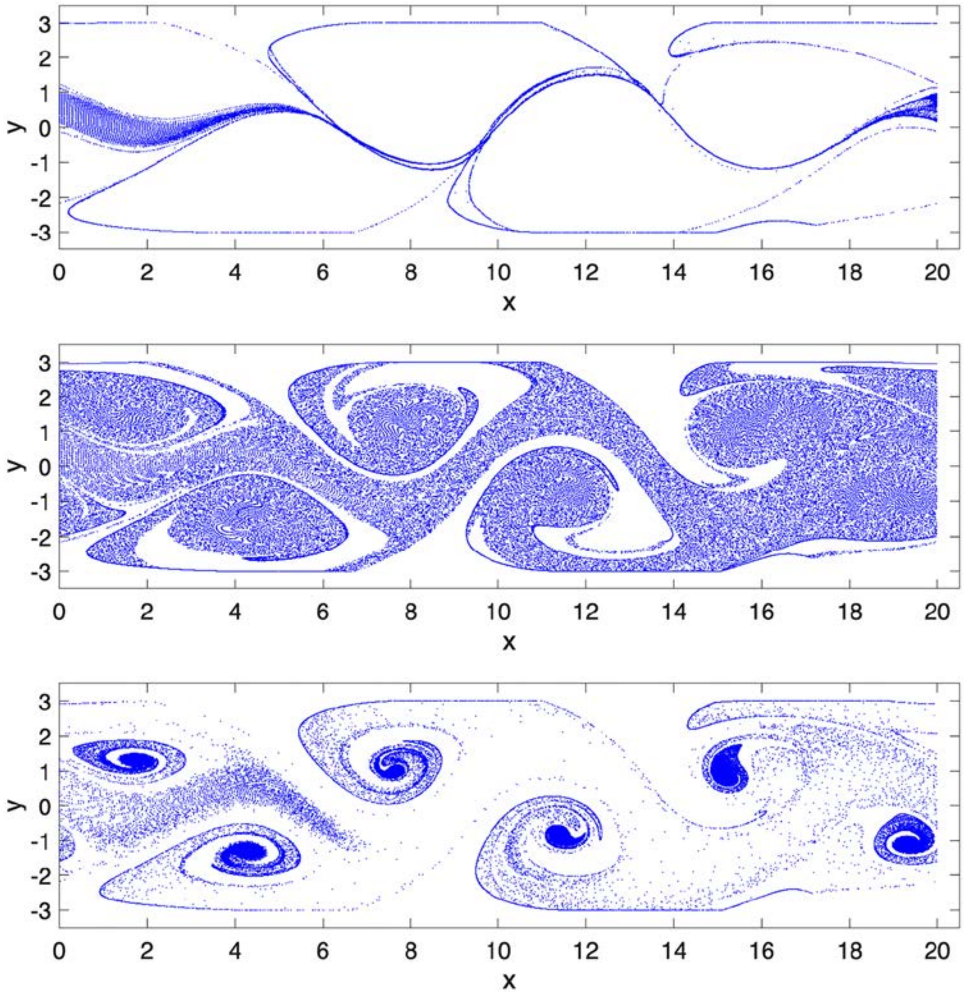

FIG. 11. Preferential aggregation of inertial particles in a Bickley jet at $t = 10$ with $St = 0.2$ for (top) aerosols ($R = 0$), (middle) neutrally buoyant particles ($R = 2/3$), and (bottom) bubbles ($R = 1$).

eddy-quadrupole flow is given as

$$\psi(x, y, t) = \left(xy\left(\sigma(t) - x^2\right) - \alpha xy^3 + \beta xy^5\right) e^{-\left(x^4+y^4\right)/\delta^4}, \quad (26)$$

where the time dependence is

$$\sigma(t) = 2\left(\arctan(10t) + \pi/2 - 1\right), \quad (27)$$

and α, β, and δ are constant parameters. The velocity field for the eddy-quadrupole flow is obtained by differentiating the stream function so that $\dot{x} = \frac{\partial\psi}{\partial y}, \dot{y} = -\frac{\partial\psi}{\partial x}$.

1. FTLE field

The FTLE field is computed to identify the coherent structures associated with the eddy-quadrupole flow. We initialized 1000×1000 passive tracer particles uniformly on a $[-3, 3] \times [-5, 5]$ grid, and the velocity field was obtained by computing derivatives of the stream function using central finite differences. Using a fourth-order Runge–Kutta method with a time integration step size of 0.01, we calculated the non-inertial particle trajectories by advecting the particles according to the velocity field. If a particle exits the flow field, the FTLE field is computed based on the particle's position on the boundary. The FTLE fields are computed using Eq. (2) and the procedure described in Sec. II A.

Figure 13 shows the backward-time FTLE field for the eddy-quadrupole flow. In a backward-time FTLE field, the maximal FTLE ridges represent attracting LCSs. These structures act as barriers that attract nearby particles as one looks backward in time. As seen in Fig. 13, and consistent with Ref. 55, there are maximal FTLE ridges surrounding the four eddies with a clear demarcation of the four eddies. One can also see FTLE ridges outside of the four eddies. These attracting structures help to identify regions

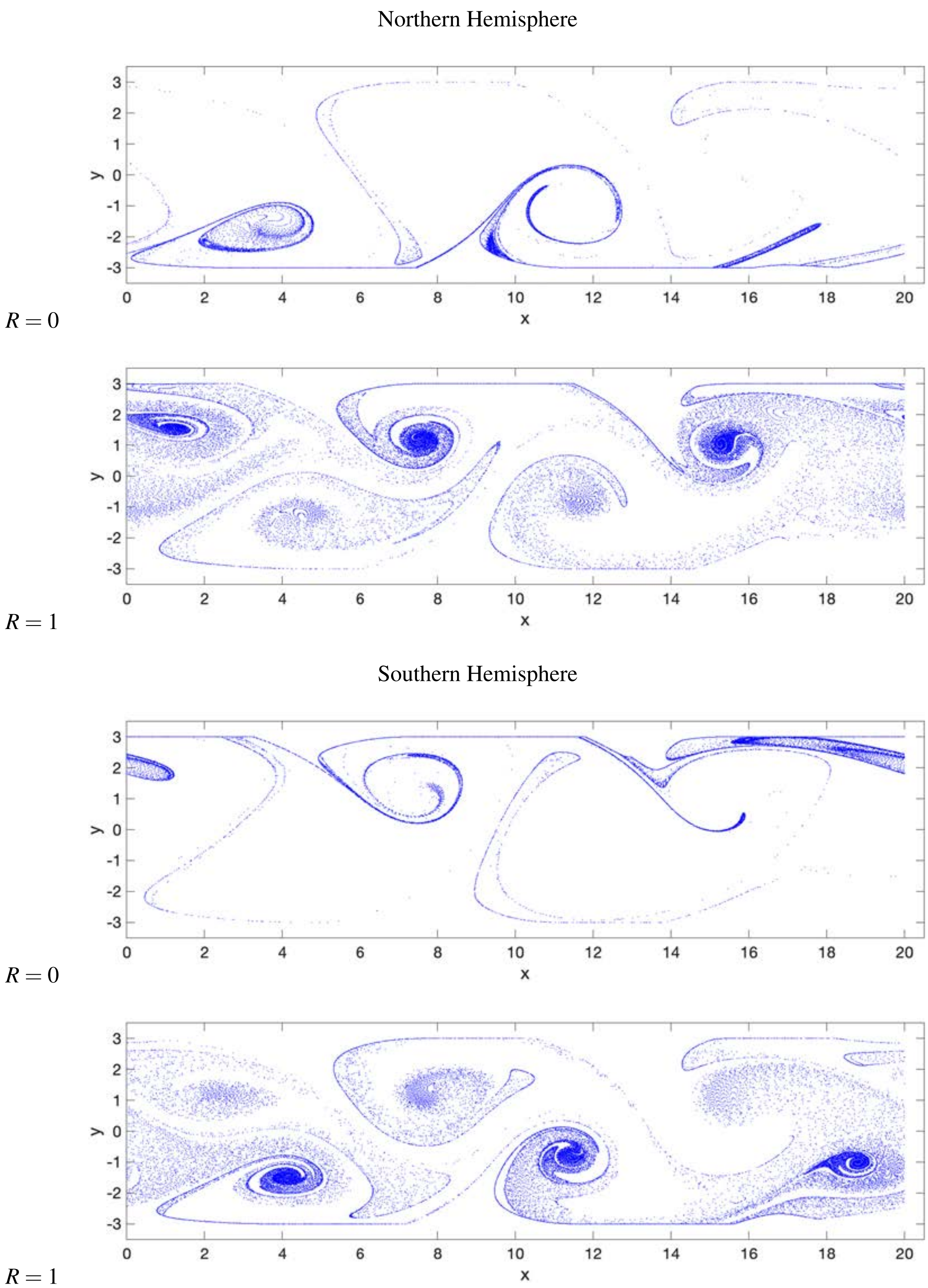

FIG. 12. Preferential aggregation of inertial particles at $t = 10$ in a Bickley jet including the Coriolis force at latitude $|\varphi| = \pi/3$ in the Northern and Southern Hemispheres for a timescale of 20 000 s at $St = 0.1$. Top two panels show (top) aerosols ($R = 0$) and (bottom) bubbles ($R = 1$) in the Northern Hemisphere; bottom two panels show the same for the Southern Hemisphere.

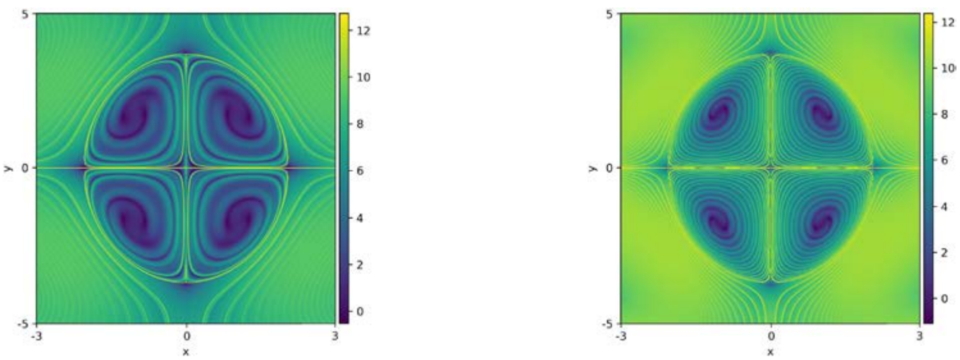

FIG. 13. Backward-time FTLE field for non-inertial particles in an eddy-quadrupole flow at (left) initial time $t_0 = 3$ for $T = -3$, and (right) at initial time $t_0 = 10$ for $T = -10$. Parameter values are $\alpha = 1/3$, $\beta = 0.008/5$, and $\delta = 5$.

within a flow field where particles are bound by coherent vortices or trapped within the quadrupole. The eddies themselves act as particle transport barriers within the flow.

2. iFTLE field

To analyze the dynamics of inertial particles in the eddy-quadrupole flow, we computed the iFTLE field for varying Stokes numbers and density ratios as in the DG flow and Bickley jet. Because the stream function includes an exponential decay term, $e^{-(x^4+y^4)/\delta^4}$, the flow velocities become negligible for $|x|, |y| > 9$. We, therefore, use a computational grid over the domain $[-9, 9] \times [-9, 9]$, which effectively captures the entire flow field. We initialized 1000×1000 inertial particles uniformly over this domain and computed their trajectories using a fourth-order Runge–Kutta method with a time integration step size of 0.01, by integrating the MR

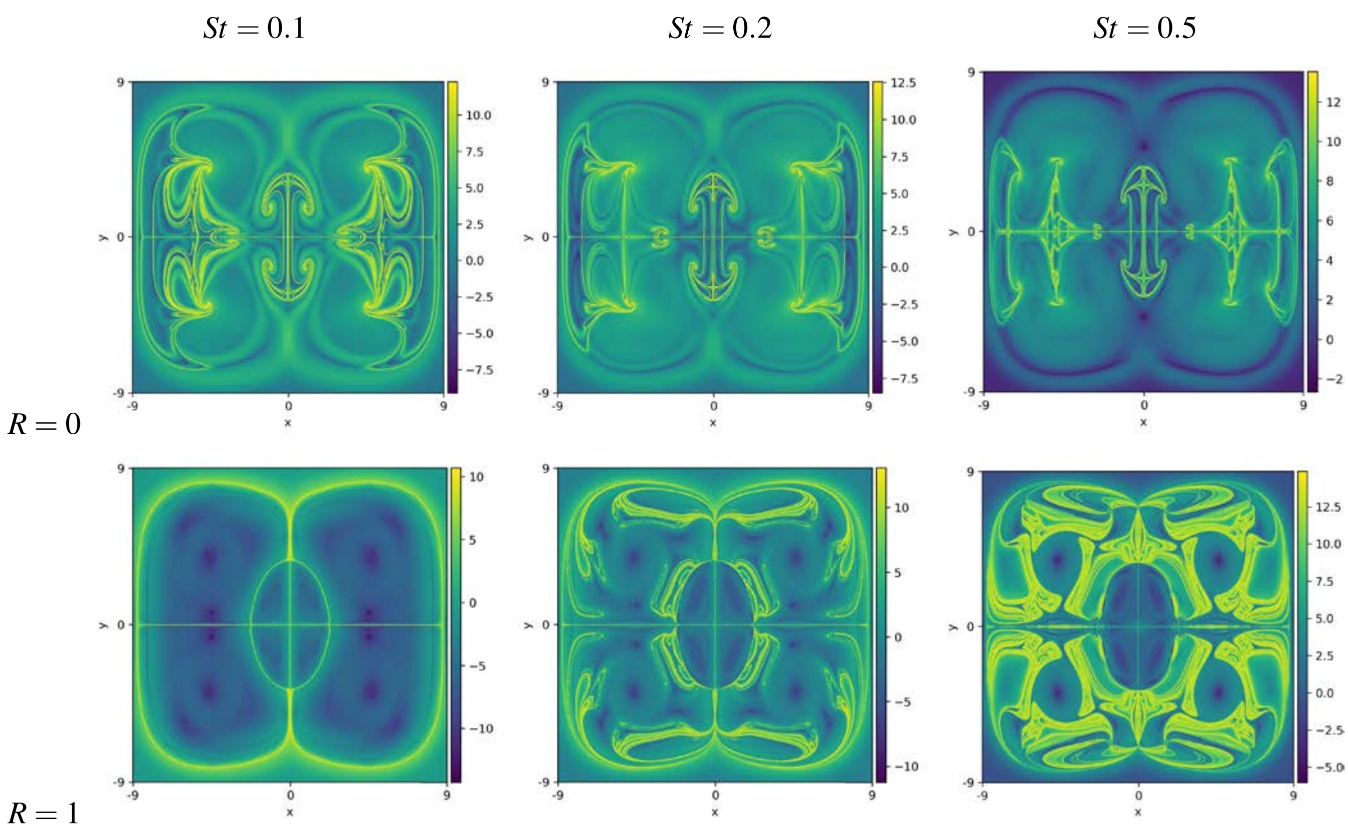

FIG. 14. Backward-time iFTLE field at initial time $t_0 = 5$ with $T = -5$ for (top) aerosols and (bottom) bubbles for a Stokes number of (left) $St = 0.1$, (middle) $St = 0.2$, and (right) $St = 0.5$ for the entire eddy-quadrupole flow field. Parameter values are $\alpha = 1/3$, $\beta = 0.008/5$, and $\delta = 5$.

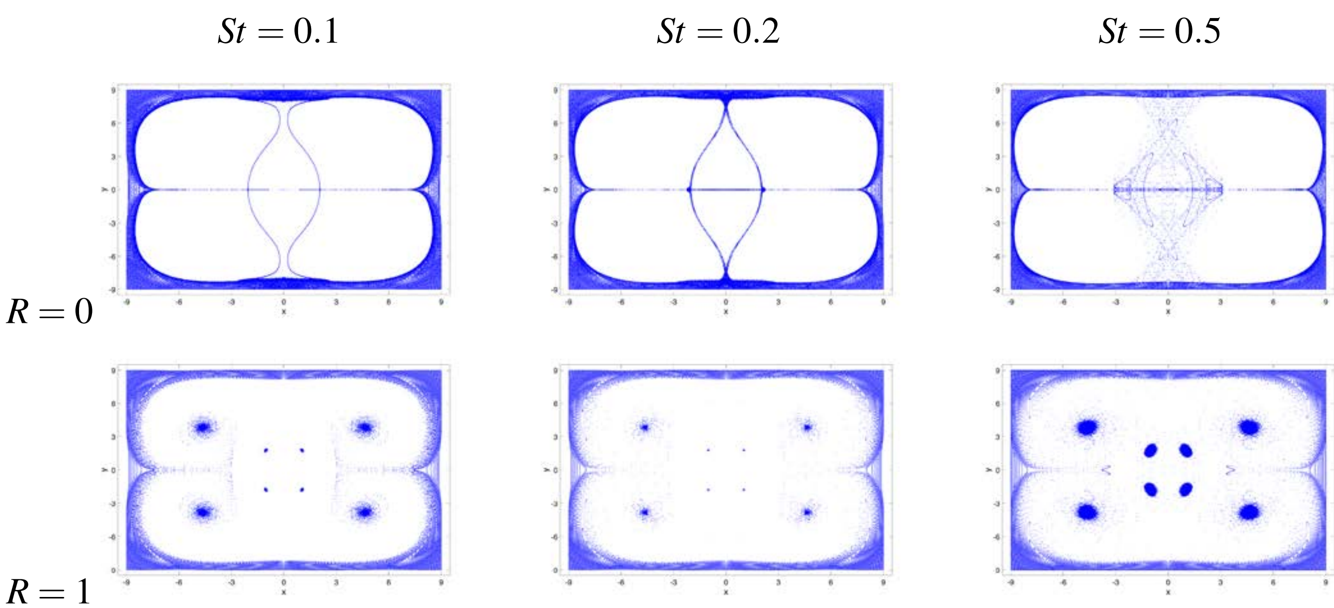

FIG. 15. Preferential aggregation of inertial particles in the eddy-quadrupole flow at $t = 5$ with $t_0 = 0$ for (top) aerosols ($R = 0$), and (bottom) bubbles ($R = 1$) for Stokes numbers of (left) $St = 0.1$, (middle) $St = 0.2$, and (right) $St = 0.5$.

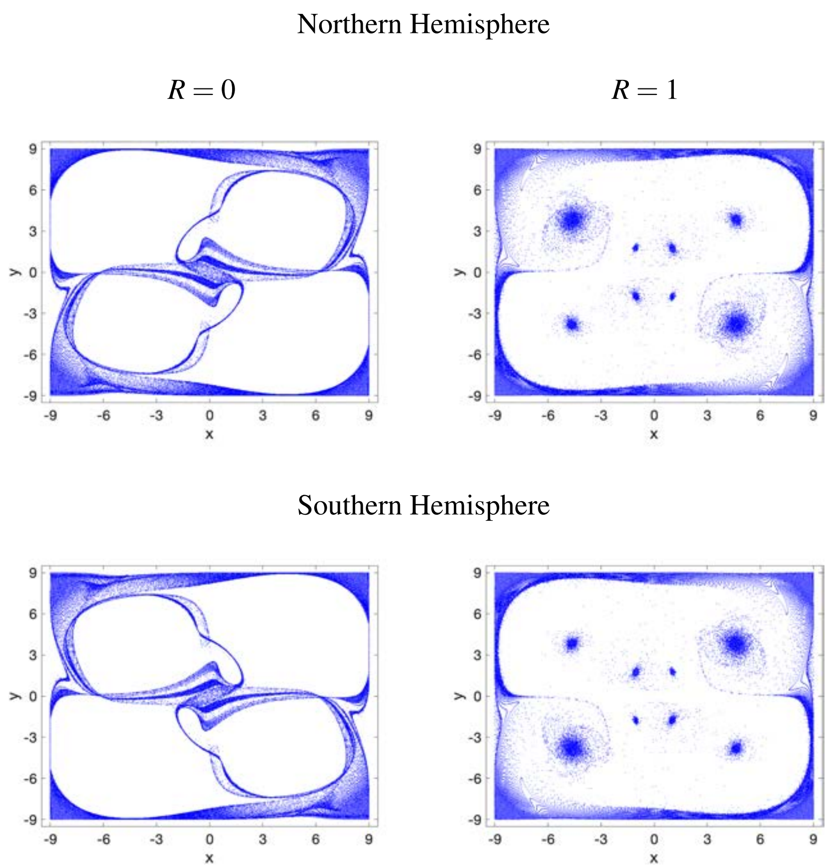

FIG. 16. Preferential aggregation of (left) aerosols ($R = 0$) and (right) bubbles ($R = 1$) at $t = 5$ with $t_0 = 0$ in an eddy-quadrupole flow including the Coriolis force at mid-latitudes ($\varphi = \pi/4$) in the Northern Hemisphere and ($\varphi = -\pi/4$) in the Southern Hemisphere for a timescale of 20 000 s at $St = 0.2$.

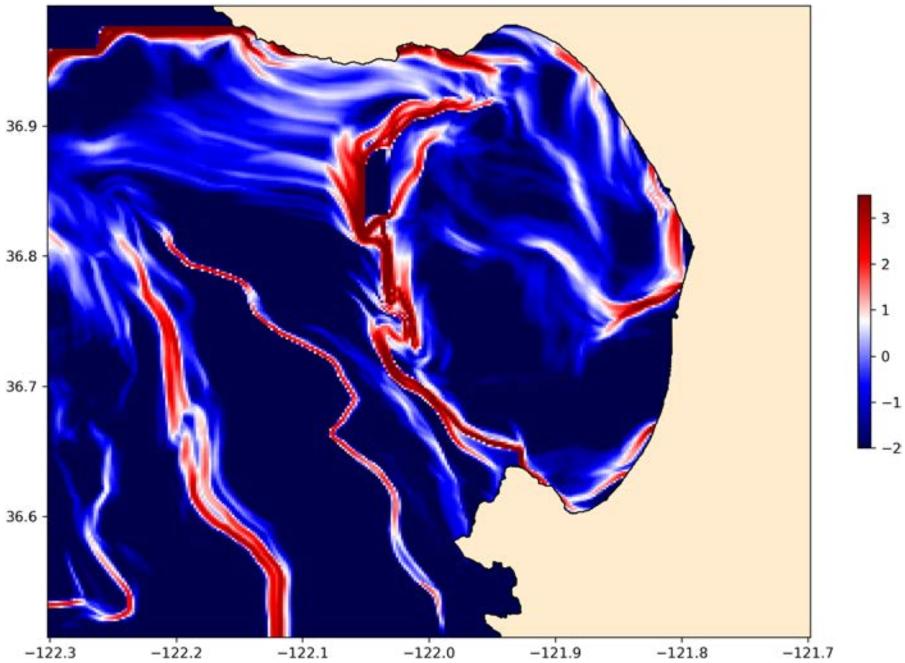

FIG. 17. Forward-time FTLE field at the initial time for the $T = 96$ h time period spanning May 1, 2020 to May 5, 2020 for the Monterey Bay region. Multimedia available online.

equation given by Eq. (11). As with non-inertial particles, if a particle exits the flow field, the iFTLE field is computed based on the particle's position on the boundary. The resulting iFTLE field is shown in Fig. 14, where one can clearly see the symmetric transition from a four-eddy to an eight-eddy configuration. The iFTLE fields on the smaller, $[-3, 3] \times [-5, 5]$ computational domain for varying Stokes numbers and density ratios are shown in Fig. 25 in Appendix D.

Figure 14 shows that the circular maximal FTLE ridges surrounding the eddies get stretched for aerosols in the iFTLE field, with the elongation becoming more discernible as the Stokes number increases. The iFTLE ridges also highlight regions where particles are no longer confined to eddies. In the case of bubbles, one can still see circular iFTLE ridges surrounding the eddies. Different from aerosols, bubbles are trapped inside the eddies, as was the case for non-inertial particles. However, as the Stokes number increases, one sees a much more complex set of iFTLE ridges outside of the four eddies. Hence, bubbles in these flow regions are no longer constrained by the eddies. Instead, they are dispersed throughout the flow, largely escaping the rotational trapping effects of the vortices. Similarly, one can clearly see the symmetric transition from four eddies to eight eddies.

3. Preferential aggregation

To explore the aggregation of inertial particles in the eddy-quadrupole flow, we consider 1000×1000 particles initialized uniformly on a $[-9, 9] \times [-9, 9]$ grid. Using a fourth-order Runge–Kutta method with a time integration step size of 0.01, the inertial particle trajectories are computed by integrating the MR equation given by Eq. (11). Figure 15 shows the preferential aggregation at $t = 5$ with $t_0 = 0$ for bubbles and aerosols for varying Stokes numbers. At low Stokes number, aerosol particles aggregate in loop-like curves around each of the four eddies. As the Stokes number increases, aerosols coalesce into a more intricate filamentary pattern, which suggests that aerosols tend to be pushed out of the eddy cores. Bubble particles, however, remain largely trapped within the eddies instead of being ejected. At low Stokes number, they form four circular clusters within each eddy core; as the Stokes number increases, more pronounced clusters appear, highlighting the eight-eddy configuration.

The thin filamentary structures in the particle aggregation of aerosols correspond to the ridges in the iFTLE plots in Fig. 14. Particles seeded anywhere in the domain are eventually pulled into these ridges. The iFTLE fields for aerosols show stronger ridges outside the eddy cores, which is consistent with the particle aggregation, where heavy particles cluster away from the eddy cores. Similarly, the aggregation of bubbles also aligns with the iFTLE ridges in Fig. 14, as the maximal iFTLE ridge encloses the eddies. As the lower iFTLE values are found inside the eddy cores, the bubbles remain trapped within or near these eddy cores, rather than being ejected as in aerosols.

4. Coriolis effect

To explore the preferential aggregation of inertial particles with the inclusion of Coriolis force in an eddy-quadrupole flow, we initialized 500×500 inertial particles on a uniform grid. Using a fourth-order Runge–Kutta method with a time integration step size of 0.01, the inertial particle trajectories are computed by integrating the MR equation given by Eq. (16). The parameter values for the eddy-quadrupole flow used in this computation are given as $\alpha = 1/3$, $\beta = 0.008/5$, and $\delta = 5$.

Figure 16 shows the preferential aggregation at $t = 5$ with $t_0 = 0$ for aerosols ($R = 0$) and bubbles ($R = 1$) at mid-latitudes for

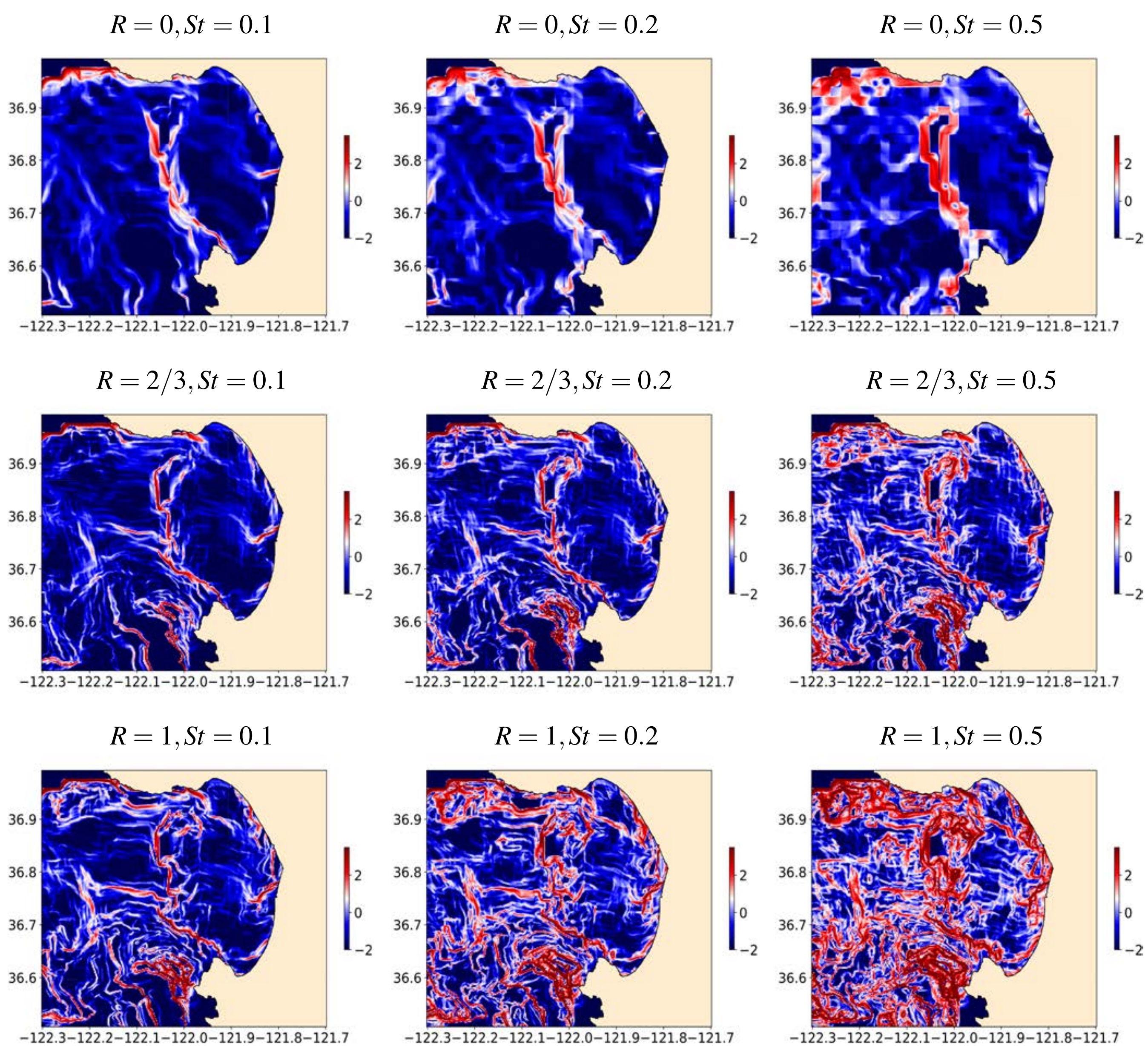

FIG. 18. Forward-time iFTLE field at the initial time for (top) aerosols, (middle) neutrally buoyant particles, and (bottom) bubbles with Stokes numbers (left column) $St = 0.1$, (middle column) $St = 0.2$, and (right column) $St = 0.5$ for the $T = 48$ h time period spanning May 1, 2020 to May 3, 2020 for the Monterey Bay region.

a representative timescale of 20 000 s and Stokes number $St = 0.2$. In the Northern Hemisphere, aerosols are expelled from the top-left and bottom-right cyclonic (counterclockwise in the Northern Hemisphere) eddies and aggregate along the boundaries of the top-right and bottom-left anticyclonic (clockwise in the Northern Hemisphere) eddies, while bubbles do the opposite, being expelled from anticyclonic eddies and clustering in the centers of cyclonic eddies. In the Southern Hemisphere, where cyclonic eddies rotate clockwise and anticyclonic eddies rotate counterclockwise, the behavior is reversed for both particle types: aerosols are expelled from cyclonic eddies and aggregate along the boundaries of anticyclonic eddies, while bubbles are expelled from cyclonic eddies and aggregate in the centers of anticyclonic eddies. This result is consistent with the theory for heavy and light particles as explained in Sec. III C 5. Preferential aggregation results for Stokes numbers $St = 0.2$ and $St = 0.5$ and Coriolis timescales 10 000 and 20 000 s for

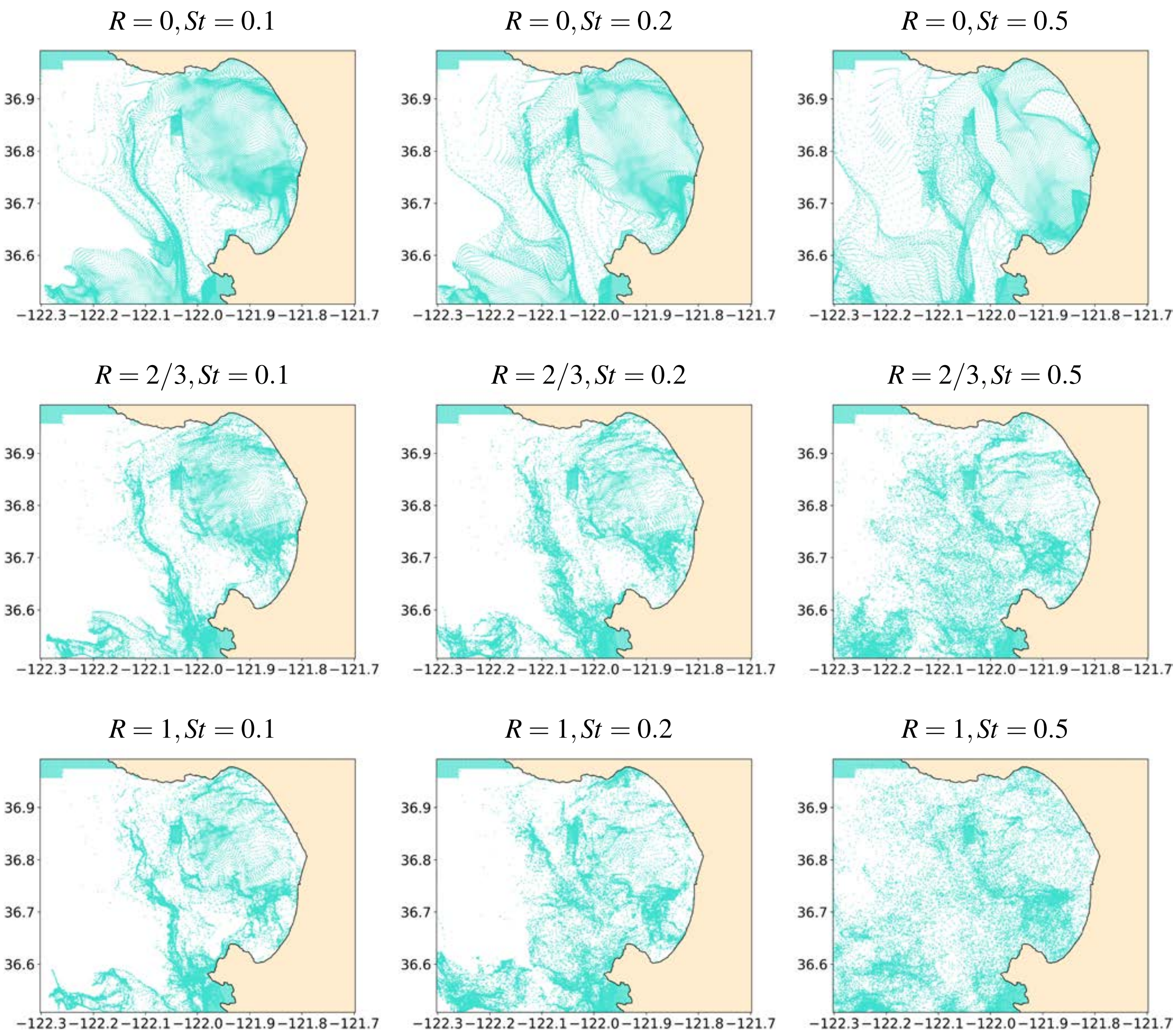

FIG. 19. Preferential aggregation of (top) aerosols, (middle) neutrally buoyant particles, and (bottom) bubbles with Stokes numbers (left column) $St = 0.1$, (middle column) $St = 0.2$, and (right column) $St = 0.5$ in Monterey Bay at $t = 96$ h for the time period spanning May 1, 2020 to May 5, 2020. Multimedia available online.

both hemispheres are shown in Figs. 26 and 27 in Appendix E. One can see that filamentary mixing structures between same-rotation eddies emerge at higher Stokes number, and aggregation toward the inertial attractors strengthens as the strength of rotation increases.

V. APPLICATION: MONTEREY BAY OCEAN DATA

As an application of our framework, we utilized ocean surface velocity data from the Monterey Bay region in California, United States of America. The data, provided by the High-Frequency Radar Network (HFRNet) under the Coastal Observing Research and Development Center (CORDC) at the University of California, San Diego (UCSD),[56] consist of 2 km resolution hourly velocity fields. Exploration of the FTLE and iFTLE fields can help identify coherent structures, which play a major role in the transport of nutrients and pollutants. By improving our understanding of the dynamics of the bay, we will be better prepared to manage the local marine ecosystem and human activities, including fishing and pollution management.

A. FTLE field

To perform the computations, we first define the Monterey Bay region based on latitude and longitude. Our choice of latitude ranges from 36.507 04° N to 36.9925° N, which captures the area from the northern part of Monterey Bay to the southern coastline. Our choice of longitude ranges from −122.301 96° W to −121.698 13° W, which includes the open ocean off the coast of Monterey Bay, as well as portions of the coastal region. To compute the non-inertial FTLE field, we initialized 300 × 280 passive tracer particles uniformly throughout the domain. Using a fourth-order Runge–Kutta method with a time integration step size of 0.01, we calculated the non-inertial particle trajectories by advecting the particles according to the ocean surface velocity field data. We use bilinear interpolation to evaluate the velocity field between grid points, while the velocity field is held constant within each hourly snapshot during the Runge–Kutta integration. If a particle exits the flow field, the FTLE field is computed based on the particle's position on the boundary. The FTLE fields are calculated using Eq. (2) and the method described in Sec. II A.

The domain includes the mouth of Monterey Bay, where significant exchange of water between the bay and the open ocean often occurs. However, as seen in Fig. 17 (Multimedia available online), sometimes there occurs a strong LCS, which serves as a transport barrier between Monterey Bay and the open ocean.

B. iFTLE field

To calculate the iFTLE field for the Monterey Bay region, we initialize 300 × 280 inertial particles uniformly over the domain as described in Sec. V A. Using a fourth-order Runge–Kutta method with a time integration step size of 0.01, the inertial particle trajectories are computed by integrating the MR equation given by Eq. (16). If a particle exits the flow field, the iFTLE field is computed based on the particle's position on the boundary.

Figure 18 shows the iFTLE field for aerosols, neutrally buoyant particles, and bubbles in the Monterey Bay region. One can see for aerosols, as for non-inertial particles in Fig. 17, a strong iFTLE ridge across the mouth of the bay. As the Stokes number increases, the iFTLE field becomes a bit more complicated, with LCS starting to radiate into the open ocean. Neutrally buoyant particles, as expected, have an iFTLE field which closely resembles the non-inertial FTLE field. As the Stokes number increases, the iFTLE field is more complicated, especially in the open ocean. In the bay itself, the LCSs governing the transport of neutrally buoyant particles are relatively consistent across different Stokes numbers. While more complicated, the iFTLE field for bubbles at low Stokes number has a similar structure to that of non-inertial particles (Fig. 17). However, as the Stokes number increases, the iFTLE ridges proliferate throughout the bay and ocean with much more complex structures.

C. Preferential aggregation of inertial particles

Figure 19 (Multimedia available online) shows the long-time distribution of aerosols, neutrally buoyant particles, and bubbles in Monterey Bay after $t = 96$ h. One can see that aerosols cluster in narrow bands rather than dispersing uniformly across the bay, mirroring the strongest iFTLE ridges in Fig. 18 and indicating that these ridges act as barriers. Neutrally buoyant particles still follow much of the ocean's circulation, so their aggregation structures resemble the non-inertial FTLE patterns shown in Fig. 17. Bubbles at low Stokes numbers aggregate in a narrow zone similar to aerosols, but they form distinct filaments in the interior of the bay at higher Stokes numbers. As the Stokes number increases, these aggregations become more filamentary, mirroring the complex web structure seen in the iFTLE fields (Fig. 18).

VI. CONCLUSIONS AND FUTURE WORK

To improve our understanding of material transport in oceanic and atmospheric flows, we have undertaken a study of the dynamics of non-inertial and inertial particles in several types of geophysical flows. For the DG, Bickley jet, and eddy-quadrupole model flows, and for real oceanic data from Monterey Bay, the underlying structures of the flow fields were examined via their associated Lagrangian coherent structures, which were found by computing the FTLE field. For inertial particles with finite size and mass, various forms of the Maxey–Riley equation were used to describe the particles' motion and to find the iFTLE field. We compared the behavior and FTLE fields of massless non-inertial particles and light (bubbles) and heavy (aerosols) inertial particles, and we explored the preferential aggregation of inertial particles in these flows. Our results

TABLE I. Summary of key findings for the double-gyre flow (Sec. III).

Effect/Parameter	Finding
Non-inertial particles	Follow LCSs
Aerosols	Aggregate along the maximal LCS between the gyres
Neutrally buoyant	Uniformly distributed throughout the flow field
Bubbles	Aggregate in the centers of both gyres
Increasing Stokes number St	Faster and more pronounced aggregation
Faxén correction	Negligible effect
D/Dt vs. d/dt assumption	Slower aggregation, but identical qualitative attractor structure
Coriolis (Northern Hemisphere)	Aerosols ejected from cyclonic to anticyclonic gyre; bubbles cluster in the center of the cyclonic gyre
Coriolis (Southern Hemisphere)	Mirror of Northern Hemisphere behavior
Increasing strength of rotation	Faster aggregation to particles' respective attractor region

TABLE II. Summary of key findings for the Bickley jet (Sec. IV).

Effect/Parameter	Finding
Non-inertial particles	Swept along the zonal jet core and into the counter-rotating vortices
Aerosols	Aggregate in the jet core; aerosol distribution around each vortex broadens leading to a visually enlarged vortex
Bubbles	Form spiral structures by blending the vortex regions with the jet core
Increasing Stokes number	More complex aerosol clustering in the jet core; pronounced spiral structures for bubbles
Coriolis (Northern Hemisphere)	Aerosols aggregate along the separatrices bounding the vortices, aggregating along the lower boundary. Bubbles form spiral structures inside the vortices and aggregate along the upper boundary
Coriolis (Southern Hemisphere)	Mirror of Northern Hemisphere behavior
Increasing strength of rotation	Faster aggregation to particles' respective attractor region

showed how particle clustering depends on the density ratio and the Stokes number.

We first considered the dynamics of non-inertial and inertial particles in a DG flow, developing a diagnostic framework through a series of parameter studies. The results showed aerosols aggregating toward the LCSs, with bubbles forming clusters at the centers of the gyres. Additionally, we explored the preferential aggregation without assuming that the total and material derivatives in the MR equation are identical. The assumption preserves the qualitative attractor structure, but particles aggregate onto their inertial attractors at a different rate. The Faxén correction has a negligible effect on the dynamics for small particles in these flows. When we included the Coriolis force, we confirmed that, in the Northern Hemisphere, heavy particles were ejected from the cyclonic gyre into the center of the anti-cyclonic gyre, while bubbles were ejected from the anti-cyclonic gyre and drawn into the cyclonic gyre. The opposite effect was seen for the Southern Hemisphere. Our results showed that the rate of aggregation onto these rotational attractors strengthens with the strength of rotation.

We then extended the analysis to the Bickley jet, a zonal flow, where the non-inertial particles were either swept along the strong jet core or moved throughout the vortices. In contrast, for inertial particles, aerosols aggregated in the strong jet core and the vortices appeared visually enlarged, covering more of the spatial domain. For bubbles, there was more of a blending of the vortices and the core, forming a spiral-like structure. FTLE fields for the Bickley jet highlighted the strong eastward zonal jet and the jet core, where the jet core acted as a particle transport barrier. The iFTLE field for aerosols highlighted the maximal iFTLE ridges inside the vortices, with low iFTLE ridges inside the jet core. Similarly, for bubbles, we found maximal iFTLE ridges around the jet core, which acted as a particle transport barrier.

Similarly, we analyzed the dynamics of non-inertial and inertial particles for an eddy-quadrupole flow. The FTLE field showed maximal ridges around the four eddies, which acted as particle transport barriers. For the iFTLE field, we observed that elongated iFTLE ridges surrounded the eddies in aerosols, whereas bubbles retained circular ridges encircling the eddies. Particle aggregation showed that aerosols formed filamentary loops outside the eddy cores, while bubbles became trapped and clustered inside the eddies.

Last, we studied non-inertial and inertial particle dynamics in the Monterey Bay region, which included the northern part of the bay to the southern coastline, part of the open ocean, and portions of the coastal region. We observed that sometimes there exists a strong

TABLE III. Summary of key findings for the eddy-quadrupole flow (Sec. IV).

Effect/Parameter	Finding
Non-inertial particles	Aggregate within flow field consisting of four eddies that smoothly transition to an eight-eddy configuration
Aerosols	Elongated iFTLE ridges around the eddies; particles form filamentary loops outside the eddy cores
Bubbles	Trapped inside the eddies, circular iFTLE ridges around each eddy
Increasing Stokes number	Filamentary mixing structures emerge between same-rotation eddies at $St = 0.5$
Coriolis (Northern Hemisphere)	Aerosols expelled from cyclonic eddies and aggregate along boundaries of anticyclonic eddies; bubbles cluster in the center of cyclonic eddies
Coriolis (Southern Hemisphere)	Mirror of Northern Hemisphere behavior
Increasing strength of rotation	Filamentary mixing between same-rotation eddies strengthens

TABLE IV. Summary of key findings for the Monterey Bay surface velocity data (Sec. V).

Effect/Parameter	Finding
Non-inertial particles	Follow ocean circulation along the coast and across the mouth of the bay; an FTLE ridge across the bay mouth separates recirculating water from open-ocean exchange
Aerosols	Have narrow bands along strong iFTLE ridges; an iFTLE ridge across the bay mouth acts as a particle transport barrier
Neutrally buoyant	Follow natural ocean circulation; LCSs proliferate at higher Stokes numbers
Bubbles	Fragment into filaments; LCSs proliferate at higher Stokes numbers, highlighting finer coastal transport structures
Increasing Stokes number *St*	Aggregation transitions from narrow bands to fragmented filamentary structures; coastal transport structures become finer and more numerous

FTLE ridge extending across the mouth of the bay, separating recirculating water from open-ocean exchange and acting as a particle transport barrier. A similar particle transport barrier was seen for aerosols with the presence of an iFTLE ridge. Meanwhile, LCSs for bubbles and neutrally buoyant particles proliferated, especially for higher Stokes numbers, highlighting finer coastal transport structures. Particle aggregation showed that aerosols traced narrow bands along strong iFTLE ridges, neutrally buoyant particles followed natural ocean circulation, and bubbles fragmented into filaments. A summary of our findings is presented in Table I (double-gyre flow), Table II (Bickley jet), Table III (eddy-quadrupole flow), and Table IV (Monterey Bay).

Taken together, we have compared and contrasted the behavior of passive tracers with that of different types of inertial particles in various flows for different forms of the MR equation. We have shown that the behavior of inertial and non-inertial particles differs markedly. The results confirm prior theoretical work and serve as a set of benchmarks across a range of fluid flows and a variety of parameter values.

In the future, it would be highly valuable to compare the results presented within this article to experimental trajectory data gathered within the lab or from drifters in the ocean. Because the MR equation is derived for small, spherical particles, one would first need to adjust for the size and shape of the drifter. Over the years, many applications involving autonomous vehicles or swarms of vehicles operating in the ocean and atmosphere have been considered. However, in much of this work, the vehicles were assumed to behave as massless particles (passive tracers). However, the inertial particle dynamics are significantly different from that of passive tracers. Moreover, even omitting or simplifying terms in the MR equation can lead to different inertial particle dynamics. This is particularly important as this can lead to prediction errors of vehicle positioning on the order of tens of kilometers in realistic coastal flows.

Also of interest in the future is the exploration of machine learning (ML) methodologies. Fueled by large volumes of data, machine learning and data analytics have revolutionized a wide range of scientific disciplines in the last few years.[57–61] We would like to extend the range of applications to the identification of coherent structures. Notably, reliable and efficient recognition of coherent structures can inform a fleet of autonomous vehicles to sample the ocean environment most effectively and, thus, can significantly advance ocean prediction. Of course, as we have demonstrated, it is critically important to include the inertial effects in these studies.

ACKNOWLEDGMENTS

This work was funded by the National Science Foundation (NSF) (Award Nos. CMMI 2121919 and 2121887).

AUTHOR DECLARATIONS

Conflict of Interest

The authors have no conflicts to disclose.

Author Contributions

Nishanta Baral: Conceptualization (equal); Data curation (lead); Formal analysis (lead); Investigation (lead); Methodology (lead); Software (lead); Validation (lead); Visualization (lead); Writing – original draft (lead); Writing – review & editing (equal). **Eric Forgoston:** Conceptualization (equal); Funding acquisition (lead); Investigation (supporting); Methodology (supporting); Project administration (lead); Supervision (lead); Writing – original draft (supporting); Writing – review & editing (equal). **M. Ani Hsieh:** Conceptualization (equal); Investigation (supporting); Methodology (supporting); Writing – review & editing (equal).

DATA AVAILABILITY

The code used to generate the double-gyre flow results in this study is openly available at https://github.com/NishantaBaral/Numerical-Study-of-MR-in-Geophysical-Flows. The remaining data that support the findings of this study are available from the corresponding author upon reasonable request.

APPENDIX A: NON-DIMENSIONALIZATION OF THE MAXEY–RILEY EQUATION

To non-dimensionalize Eq. (6), we introduce the non-dimensional variables $\hat{r}$, $\hat{u}$, and $\hat{t}$ so that $r \to \hat{r}L$, $u \to \hat{u}U$, and $t = \frac{L}{U}\hat{t}$.[37] Thus, $\dot{r} = U\hat{r}\prime$ and $\ddot{r} = \frac{U^2}{L}\hat{r}''$, where $'$ denotes $\frac{d}{d\hat{t}}$. The Faxén correction term is non-dimensionalized as $\nabla^2 u \to \frac{U}{L^2}\hat{\nabla}\hat{u}$. Writing Eq. (6) in terms of the non-dimensional scalings, one obtains

$$\begin{aligned}\frac{U^2}{L}m_p\hat{r}'' &= m_f\frac{U^2}{L}\frac{D\hat{u}}{D\hat{t}} - \frac{1}{2}m_f\frac{U^2}{L}\hat{r}'' + \frac{1}{2}m_f\frac{U^2}{L}\frac{d\hat{u}}{d\hat{t}}\\ &\quad + \frac{1}{20}m_f a^2\frac{U^2}{L^3}\frac{d(\hat{\nabla}^2\hat{u})}{d\hat{t}}\\ &\quad - 6\pi a\mu[U\hat{r}' - \hat{u}U - \frac{1}{6}a^2\frac{U}{L^2}\hat{\nabla}^2\hat{u}] + (m_p - m_f)\,g. \end{aligned} \tag{A1}$$

Collecting the $\hat{r}''$ terms on the left-hand side of Eq. (A1), one has

$$\begin{aligned}\frac{U^2}{L}m_p\hat{r}'' + \frac{1}{2}m_f\frac{U^2}{L}\hat{r}'' &= m_f\frac{U^2}{L}\frac{D\hat{u}}{D\hat{t}} + \frac{1}{2}m_f\frac{U^2}{L}\frac{d\hat{u}}{d\hat{t}}\\ &\quad + \frac{1}{20}m_f a^2\frac{U^2}{L^3}\frac{d(\hat{\nabla}^2\hat{u})}{d\hat{t}} - 6\pi a\mu[U\hat{r}' - \hat{u}U\\ &\quad - \frac{1}{6}a^2\frac{U}{L^2}\hat{\nabla}^2\hat{u}] + (m_p - m_f)\,g, \end{aligned} \tag{A2}$$

which can be rewritten as

$$\begin{aligned}&\left(\frac{U^2}{L}(m_p + \frac{1}{2}m_f)\right)\hat{r}''\\ &= m_f\frac{U^2}{L}\frac{D\hat{u}}{D\hat{t}} + \frac{1}{2}m_f\frac{U^2}{L}\frac{d\hat{u}}{d\hat{t}} + \frac{1}{20}m_f a^2\frac{U^2}{L^3}\frac{d(\hat{\nabla}^2\hat{u})}{d\hat{t}}\\ &\quad - 6\pi a\mu[U\hat{r}' - \hat{u}U - \frac{1}{6}a^2\frac{U}{L^2}\hat{\nabla}^2\hat{u}] + (m_p - m_f)\,g. \end{aligned} \tag{A3}$$

We reorder the terms in Eq. (A3) in the form of particle acceleration term = acceleration of the fluid element term + Stokes drag term + buoyancy effect term + terms involving the Faxén correction so that

$$\begin{aligned}&\left(\frac{U^2}{L}\left(m_p + \frac{1}{2}m_f\right)\right)\hat{r}''\\ &= m_f\frac{U^2}{L}\frac{D\hat{u}}{D\hat{t}} + \frac{1}{2}m_f\frac{U^2}{L}\frac{d\hat{u}}{d\hat{t}} - 6\pi a\mu U[\hat{r}' - \hat{u}] + (m_p - m_f)\,g\\ &\quad + \frac{1}{20}m_f a^2\frac{U^2}{L^3}\frac{d(\hat{\nabla}^2\hat{u})}{d\hat{t}} + \pi a\mu a^2\frac{U}{L^2}\hat{\nabla}^2\hat{u}, \end{aligned} \tag{A4}$$

which can be rewritten as

$$\begin{aligned}\hat{r}'' &= \frac{m_f\frac{U^2}{L}}{\left(\frac{U^2}{L}(m_p + \frac{1}{2}m_f)\right)}\frac{D\hat{u}}{D\hat{t}} + \frac{m_f\frac{U^2}{L}}{\left(\frac{U^2}{L}(m_p + \frac{1}{2}m_f)\right)}\frac{1}{2}\frac{d\hat{u}}{d\hat{t}}\\ &\quad + \frac{6\pi a\mu U}{\left(\frac{U^2}{L}(m_p + \frac{1}{2}m_f)\right)}[\hat{u} - \hat{r}'] + \frac{(m_p - m_f)}{\left(\frac{U^2}{L}(m_p + \frac{1}{2}m_f)\right)}g\\ &\quad + \frac{\frac{1}{20}m_f a^2\frac{U^2}{L^3}\frac{d(\hat{\nabla}^2\hat{u})}{d\hat{t}}}{\left(\frac{U^2}{L}(m_p + \frac{1}{2}m_f)\right)} + \frac{\pi a\mu a^2\frac{U}{L^2}\hat{\nabla}^2\hat{u}}{\left(\frac{U^2}{L}(m_p + \frac{1}{2}m_f)\right)}. \end{aligned} \tag{A5}$$

Further algebraic simplification of Eq. (A5) leads to

$$\begin{aligned}\hat{r}'' &= \frac{m_f}{(m_p + \frac{1}{2}m_f)}\frac{D\hat{u}}{D\hat{t}} + \frac{m_f}{(m_p + \frac{1}{2}m_f)}\frac{1}{2}\frac{d\hat{u}}{d\hat{t}} + \frac{6\pi a\mu L}{U(m_p + \frac{1}{2}m_f))}[\hat{u} - \hat{r}']\\ &\quad + \frac{(m_p - m_f)}{\left(\frac{U^2}{L}(m_p + \frac{1}{2}m_f)\right)}g + \frac{1}{20}\frac{a^2}{L^2}\frac{m_f}{m_p + \frac{1}{2}m_f}\frac{d(\hat{\nabla}^2\hat{u})}{d\hat{t}}\\ &\quad + \frac{1}{6}\frac{a^2}{L^2}\frac{6\pi a\mu L}{U(m_p + \frac{1}{2}m_f)}\hat{\nabla}^2\hat{u}. \end{aligned} \tag{A6}$$

The non-dimensional MR equation, including buoyancy and the Faxén correction, is given as

$$\begin{aligned}\hat{r}''(t) &= R\frac{D}{D\hat{t}}\hat{u}(r(\hat{t}),\hat{t}) + \frac{1}{2}R\frac{d}{d\hat{t}}\hat{u}(r(\hat{t}),\hat{t}) + \frac{1}{St}[\hat{u}(r(\hat{t}),\hat{t}) - \hat{r}'(\hat{t})]\\ &\quad + Wn + \frac{1}{20}P^2R\frac{d(\hat{\nabla}^2\hat{u})}{d\hat{t}} + \frac{1}{6}\frac{P^2}{St}\hat{\nabla}^2\hat{u}, \end{aligned} \tag{A7}$$

where

$$\begin{aligned}St^{-1} &= \frac{6\pi a\mu L}{(m_p + \frac{1}{2}m_F)\,U}, \quad R = \frac{m_f}{m_p + \frac{1}{2}m_f},\\ W &= \frac{m_p - m_f}{6\pi a\mu USt}g, \quad \text{and} \quad P = \frac{a}{L}. \end{aligned} \tag{A8}$$

Ignoring buoyancy, this non-dimensional form is also provided as Eq. (9).

APPENDIX B: ADDITIONAL PREFERENTIAL AGGREGATION RESULTS FOR THE DOUBLE-GYRE FLOW

This appendix provides supplementary results for the DG flow, complementing the analysis in Sec. III C. The computational setup is identical to that previously described.

1. Preferential aggregation for varying density ratios

Figure 20 shows the preferential aggregation of inertial particles at $t = 15$ for a fixed Stokes number $St = 0.5$ and different density ratios ranging from aerosols ($R = 0$) to bubbles ($R = 1$). One can see that aerosols aggregate toward the maximal iFTLE ridges while bubbles ($R = 1$) are repelled from the maximal iFTLE ridges, forming clusters in the center of the gyres instead. Neutrally buoyant particles ($R = 2/3$) follow the underlying flow without preferential clustering.

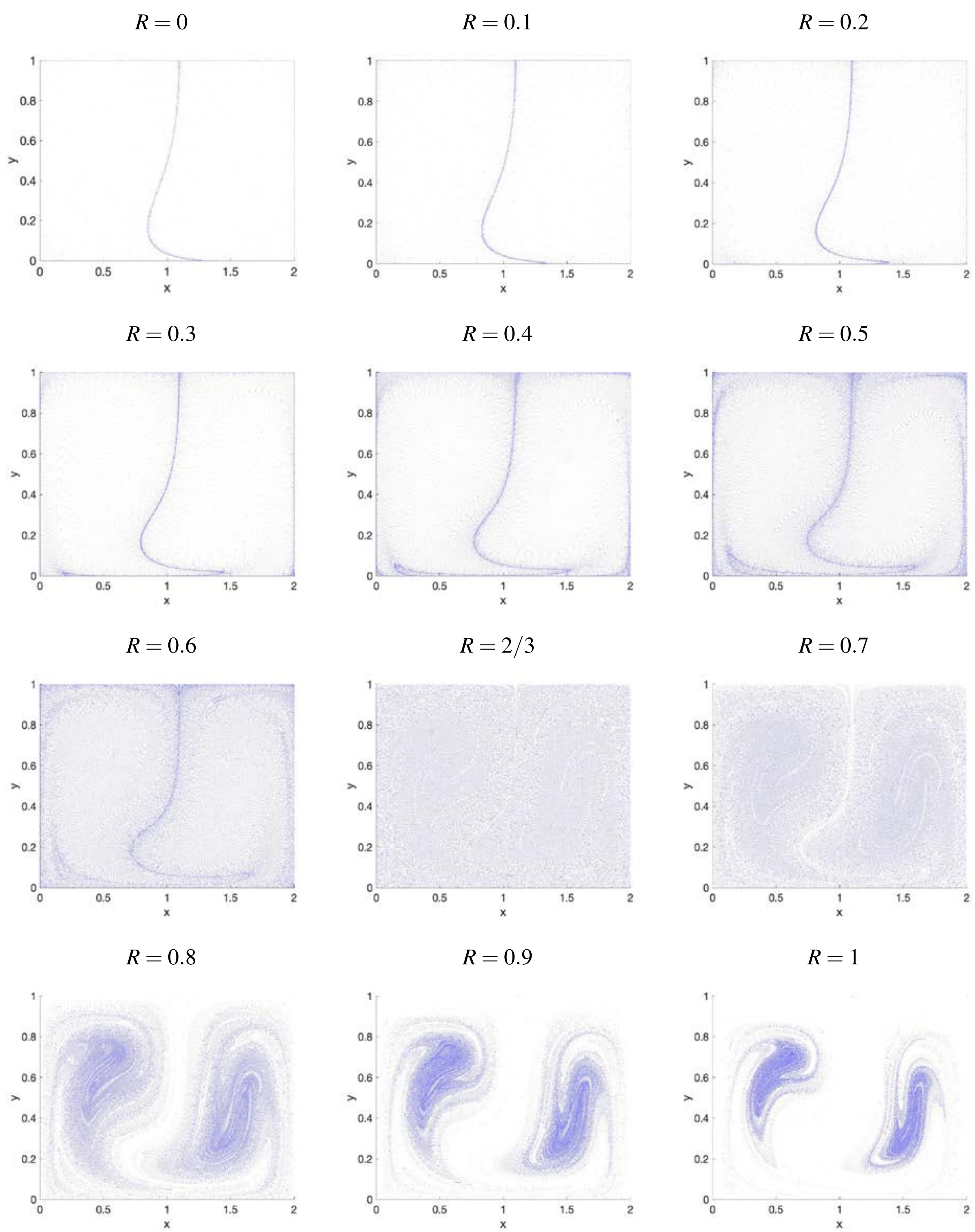

FIG. 20. Preferential aggregation for inertial particles at $t = 15$ for $St = 0.5$ and varying density ratios. The parameter values for the double-gyre flow used in the computation are $A = 0.1$, $\omega = 6\pi/10$, and $\varepsilon = 0.25$.

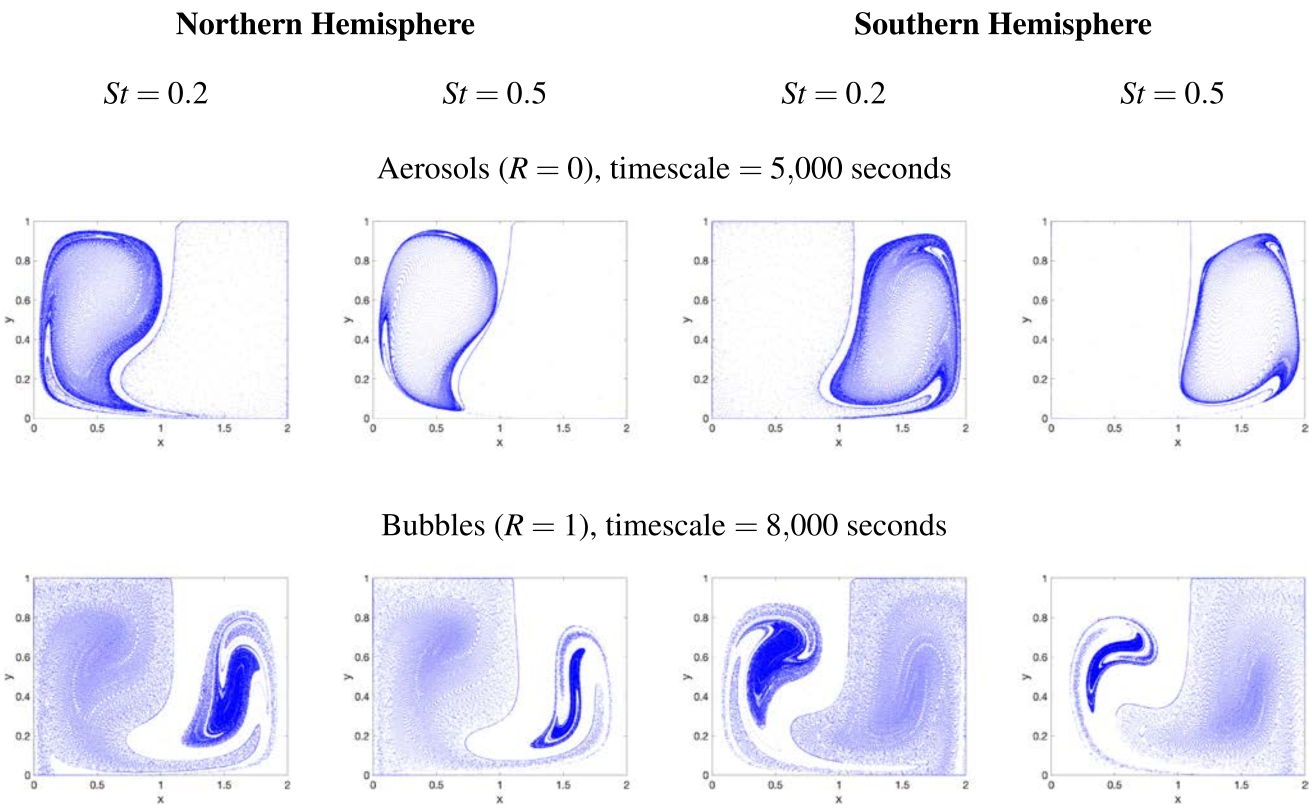

FIG. 21. Preferential aggregation at $t = 15$ in a double-gyre flow including the Coriolis force at mid-latitudes for (top row) aerosols ($R = 0$) with a Coriolis non-dimensionalization timescale of 5000 s, and (bottom row) bubbles ($R = 1$) with a timescale of 8000 s. The left two columns represent the Northern Hemisphere ($\varphi = \pi/4$) and the right two columns represent the Southern Hemisphere ($\varphi = -\pi/4$). Within each hemisphere block, the Stokes numbers are $St = 0.2$ (left) and $St = 0.5$ (right).

2. Preferential aggregation for Coriolis effect

Figure 21 shows the preferential aggregation of aerosols and bubbles in the DG flow with the inclusion of the Coriolis force at additional values of the Coriolis non-dimensionalization timescale, complementing the results shown in Fig. 8 of Sec. III C 5. For aerosols (top row), in both hemispheres particles are expelled from cyclonic gyres and accumulate in anticyclonic ones, with more pronounced aggregation at higher Stokes number. For bubbles (bottom row), they cluster in cyclonic gyre centers in the Northern Hemisphere and anticyclonic gyre centers in the Southern Hemisphere. This is consistent with the preferential aggregation of aerosols and bubbles as seen in the main text.

APPENDIX C: ADDITIONAL PREFERENTIAL AGGREGATION RESULTS FOR THE BICKLEY JET

This appendix provides supplementary results for the Bickley jet, complementing the analysis in Sec. IV A.

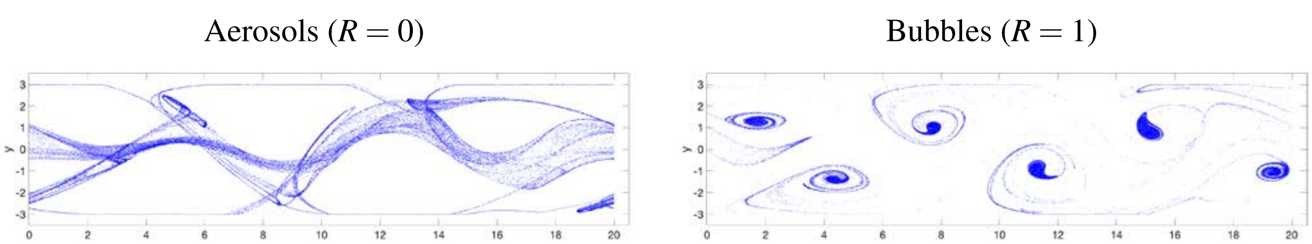

FIG. 22. Preferential aggregation of inertial particles for (left) aerosols ($R = 0$), and (right) bubbles ($R = 1$) in a Bickley jet flow model at time $t = 10$ with $St = 0.5$.

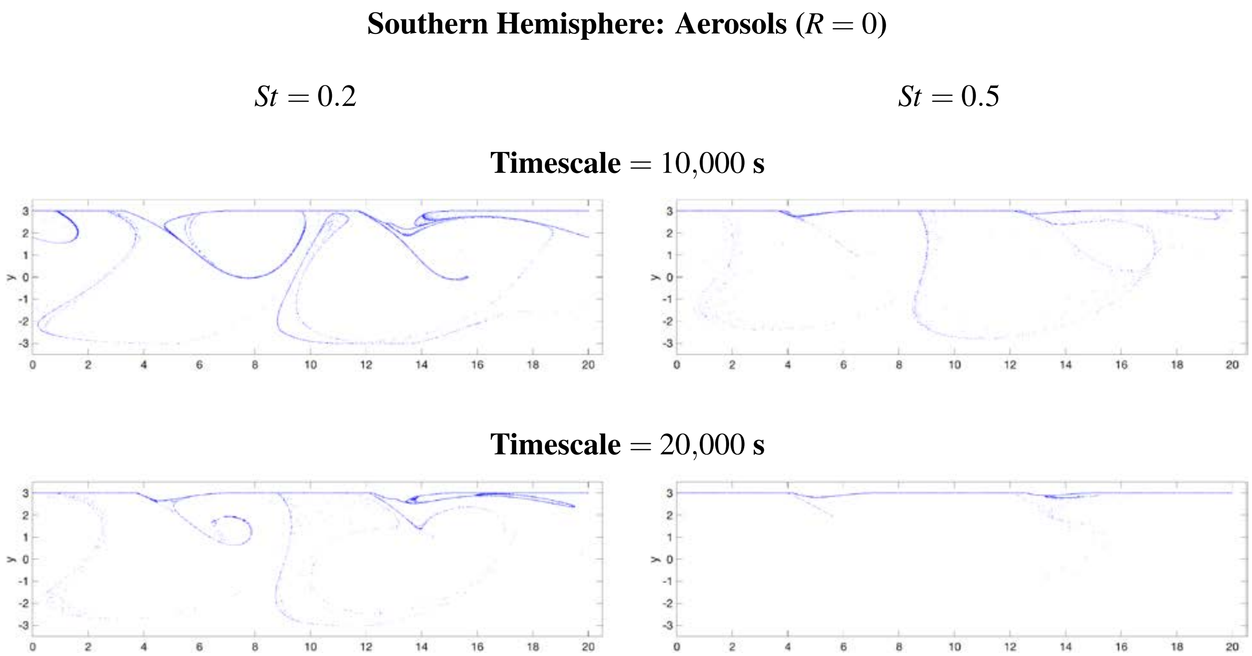

FIG. 23. Preferential aggregation for aerosols ($R = 0$) in a Bickley jet including the Coriolis force in the Southern Hemisphere ($\varphi = -\pi/3$). The left column shows $St = 0.2$ and the right column shows $St = 0.5$, for non-dimensionalization timescales of 10 000 s (top row) and 20 000 s (bottom row).

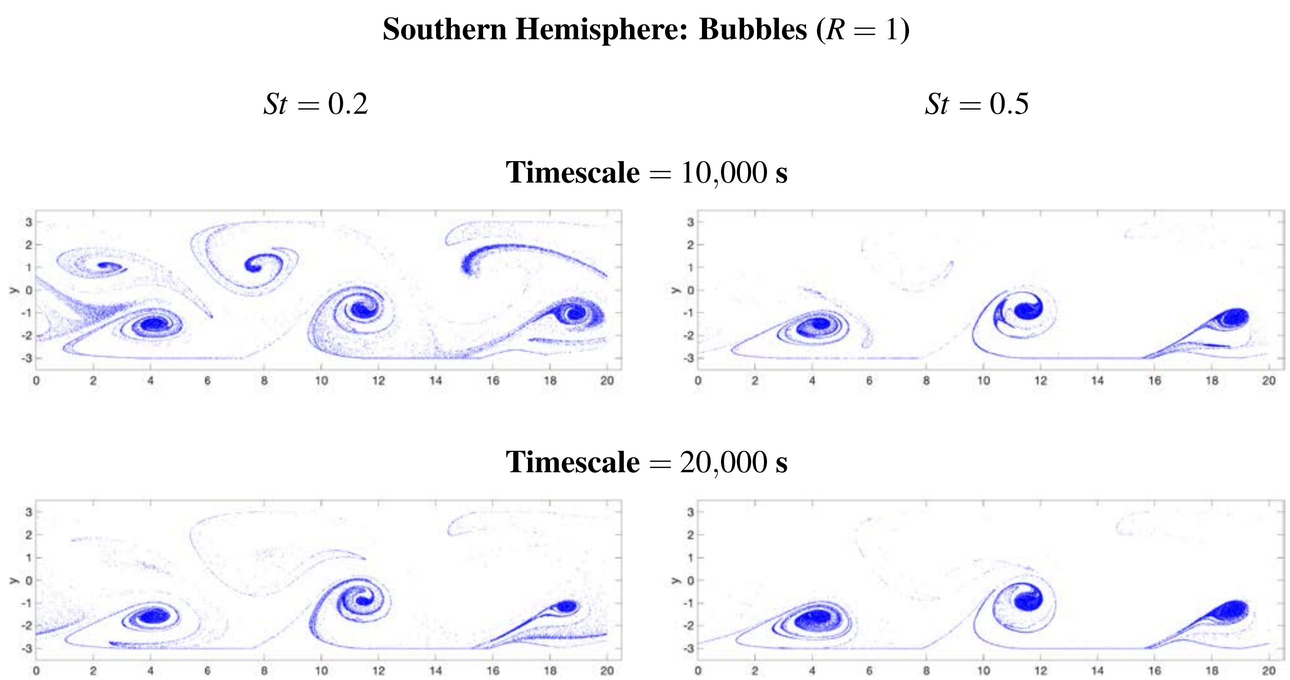

FIG. 24. Preferential aggregation for bubbles ($R = 1$) in a Bickley jet including the Coriolis force in the Southern Hemisphere ($\varphi = -\pi/3$). The left column shows $St = 0.2$ and the right column shows $St = 0.5$, for non-dimensionalization timescales of 10 000 s (top row) and 20 000 s (bottom row).

1. Preferential aggregation for higher Stokes number

Figure 22 shows the preferential aggregation of aerosols and bubbles in the Bickley jet for $St = 0.5$, complementing the results shown in Fig. 11 in Sec. IV A. Figure 22 shows that as the Stokes number is increased from $St = 0.2$ to $St = 0.5$, one finds similar but more pronounced spiral behavior for bubbles. Aerosol aggregation, while still mostly occurring in the jet core, is more complicated, commensurate with the more complicated iFTLE field shown in Fig. 10 for $St = 0.5$.

2. Preferential aggregation for Coriolis effect

Figure 12 in Sec. IV A 4 shows the aggregation of particles in the Bickley jet with Coriolis force for $St = 0.1$ in both hemispheres. As a complement, Figs. 23 and 24 show the preferential aggregation for $St = 0.1$, $St = 0.2$, and $St = 0.5$ at two different Coriolis timescales (10 000 and 20 000 s). Because the Bickley jet parameters used in this work are specifically tuned to model the stratospheric polar night jet in the Southern Hemisphere, we present the extended results exclusively for the Southern Hemisphere. As demonstrated in the main text, a complete hemispheric reversal is expected for the Northern Hemisphere. The results are consistent with Fig. 12, with aerosols increasingly swept to the boundary at higher Stokes numbers and aggregation toward the inertial attractors strengthening as the Coriolis timescale increases.

APPENDIX D: ADDITIONAL iFTLE RESULTS FOR THE EDDY-QUADRUPOLE FLOW

Figure 14 in Sec. IV B 1 shows the iFTLE field on the domain $[-9, 9] \times [-9, 9]$ in order to capture the full extent of the eddy-quadrupole flow. As a complement, Fig. 25 shows the backward-time iFTLE fields on the smaller, $[-3, 3] \times [-5, 5]$ domain, where one can clearly see the four eddy configurations.

Figure 25 shows that the circular maximal FTLE ridges surrounding the eddies become elongated for aerosols, with the elongation more pronounced as the Stokes number increases. The iFTLE ridges also highlight regions where particles are no longer confined to the eddies. For bubbles, circular iFTLE ridges surrounding the eddies remain visible. Unlike aerosols, bubbles are trapped inside the eddies, as was the case for non-inertial particles. However, as the Stokes number increases, a more complex set of iFTLE ridges emerges outside the four eddies, indicating that bubbles in these regions are no longer constrained by the eddies and are instead dispersed throughout the flow, largely escaping the rotational trapping effects of the vortices.

APPENDIX E: PREFERENTIAL AGGREGATION IN AN EDDY-QUADRUPOLE FLOW WITH THE CORIOLIS FORCE

Figure 16 in Sec. IV B 4 shows the aggregation of particles in the eddy-quadrupole flow with Coriolis force for $St = 0.2$ for one choice of Coriolis timescale. As a complement, Figs. 26 and 27 show the aggregation for $St = 0.2$ and $St = 0.5$ at two Coriolis timescales (10 000 and 20 000 s) in both hemispheres.

Figures 26 and 27 show the preferential aggregation of aerosols ($R = 0$) and bubbles ($R = 1$), respectively, at $t = 5$ with $t_0 = 0$. The preferential aggregation behavior described in Sec. IV B 4 is seen at all parameter values; however, at $St = 0.5$, filamentary mixing structures appear between same-rotation eddies connecting the two

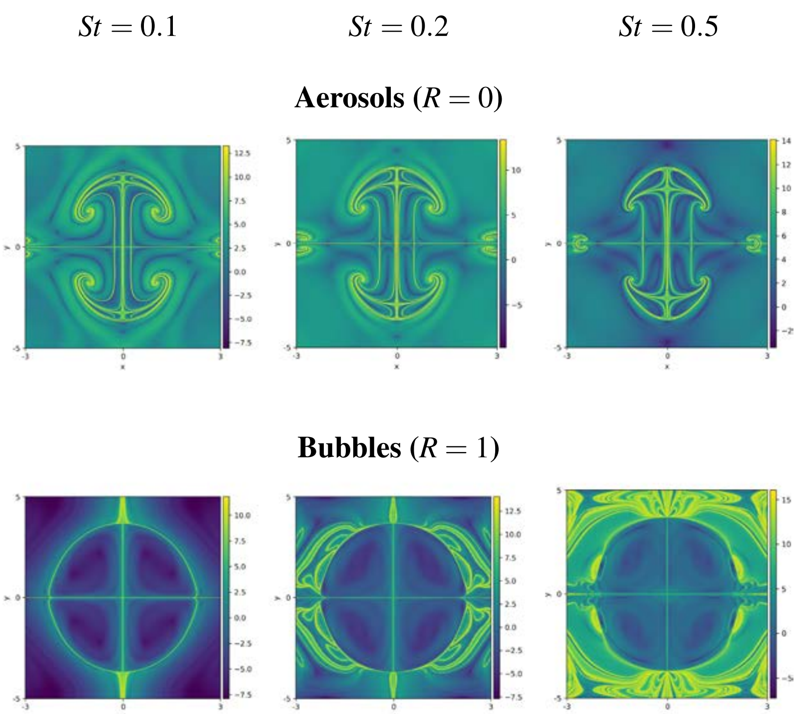

FIG. 25. Backward-time iFTLE field at initial time $t_0 = 5$ with $T = -5$ on the smaller domain $[-3, 3] \times [-5, 5]$ for (top) aerosols and (bottom) bubbles for Stokes numbers (left) $St = 0.1$, (middle) $St = 0.2$, and (right) $St = 0.5$. Parameter values are $\alpha = 1/3$, $\beta = 0.008/5$, and $\delta = 5$.

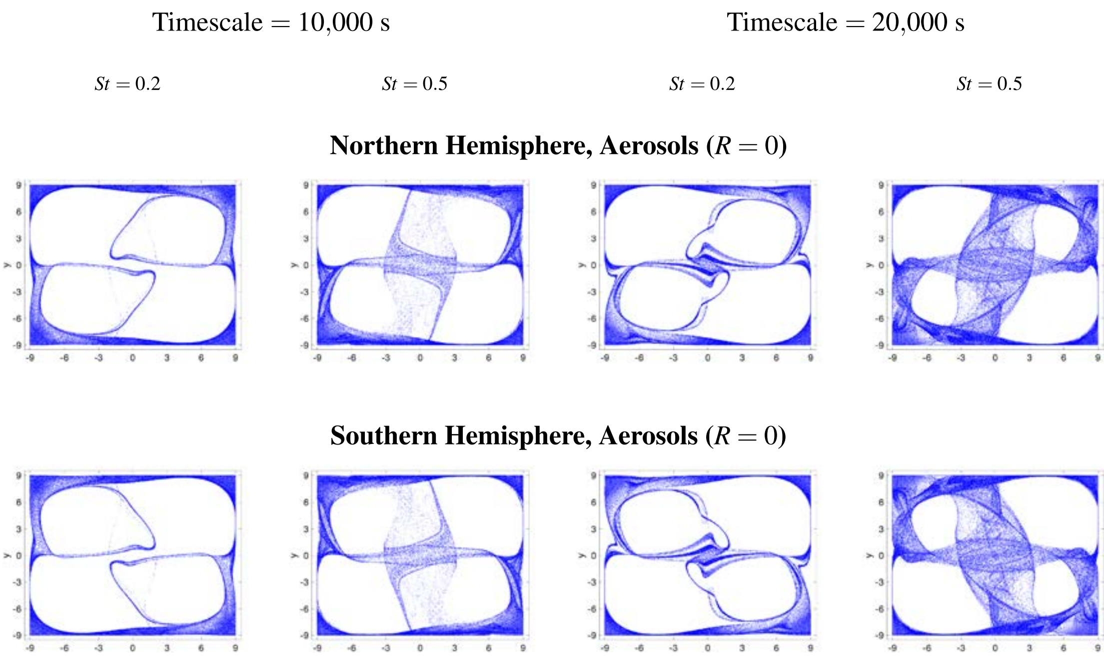

FIG. 26. Preferential aggregation of aerosols ($R = 0$) at $t = 5$ in an eddy-quadrupole flow. The grid is organized by Northern (top row) and Southern (bottom row) Hemisphere. Columns represent increasing Stokes numbers ($St = 0.2/0.5$) within the 10 000 s timescale block (left two columns) and the 20 000 s timescale block (right two columns).

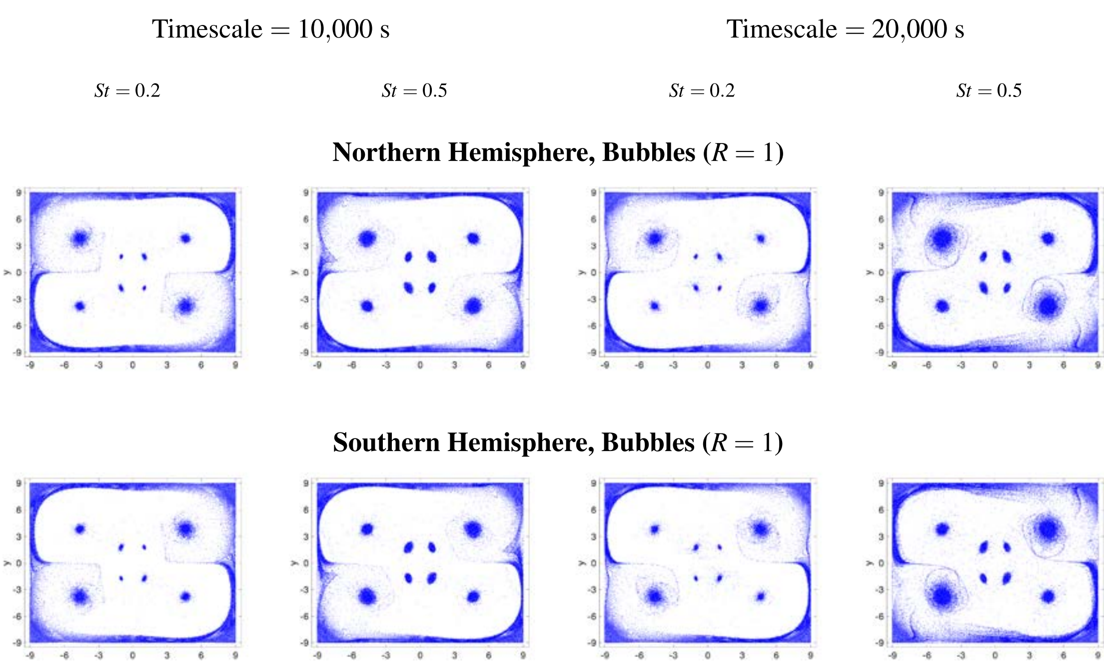

FIG. 27. Preferential aggregation parameter sweep of bubbles ($R = 1$) at $t = 5$ in an eddy-quadrupole flow. The grid is organized by Northern (top row) and Southern (bottom row) Hemisphere. Columns represent increasing Stokes numbers ($St = 0.2/0.5$) within the 10 000 s timescale block (left two columns) and the 20 000 s timescale block (right two columns).

anticyclonic eddies in the Northern Hemisphere for aerosols, and the two cyclonic eddies in the Southern Hemisphere. Similarly, increasing the Coriolis timescale results in more pronounced aggregation toward the inertial attractors for both aerosols and bubbles. These results remain consistent with the theory for heavy and light particles as explained in Sec. III C 5.

REFERENCES

[1] M. Michini, M. A. Hsieh, E. Forgoston, and I. B. Schwartz, "Robotic tracking of coherent structures in flows," IEEE Trans. Robot. **30**(3), 593–603 (2014).
[2] E. Forgoston, L. Billings, P. Yecko, and I. B. Schwartz, "Set-based corral control in stochastic dynamical systems: Making almost invariant sets more invariant," Chaos **21**(1), 013116 (2011).
[3] E. Tew Kai, V. Rossi, J. Sudre, H. Weimerskirch, C. Lopez, E. Hernandez-Garcia, F. Marsac, and V. Garçon, "Top marine predators track Lagrangian coherent structures," Proc. Natl. Acad. Sci. U.S.A. **106**(20), 8245–8250 (2009).
[4] A. E. Bozorg Magham, S. D. Ross, and D. G. Schmale III, "Real-time prediction of atmospheric Lagrangian coherent structures based on forecast data: An application and error analysis," Physica D **258**, 47–60 (2013).
[5] R. B. Husar, D. Tratt, B. A. Schichtel, S. Falke, F. Li, D. Jaffe, S. Gasso, T. Gill, N. S. Laulainen, F. Lu *et al.*, "Asian dust events of April 1998," J. Geophys. Res.: Atmos. **106**(D16), 18317–18330, https://doi.org/10.1029/2000JD900788 (2001).
[6] P. J. Nolan, H. Foroutan, and S. D. Ross, "Pollution transport patterns obtained through generalized Lagrangian coherent structures," Atmosphere **11**(2), 168 (2020).
[7] A. Stohl, S. Eckhardt, C. Forster, P. James, and N. Spichtinger, "On the pathways and timescales of intercontinental air pollution transport," J. Geophys. Res.: Atmos. **107**(D23), ACH-6, https://doi.org/10.1029/2001JD001396 (2002).
[8] Copernicus Atmosphere Monitoring Service, "Smoke from Canadian wildfires reaches Europe," see https://atmosphere.copernicus.eu/smoke-canadian-wildfires-reaches-europe (last accessed May 22, 2025).
[9] Y. Liu, C. Wilson, M. A. Green, and C. W. Hughes, "Gulf Stream transport and mixing processes via coherent structure dynamics," J. Geophys. Res.: Oceans **123**(4), 3014–3037, https://doi.org/10.1002/2017JC013390 (2018).
[10] C. W. Böning, A. Dispert, M. Visbeck, S. Rintoul, and F. U. Schwarzkopf, "The response of the Antarctic Circumpolar Current to recent climate change," Nat. Geosci. **1**(12), 864–869 (2008).
[11] G. Haller, "Lagrangian coherent structures," Annu. Rev. Fluid Mech. **47**, 137–162 (2015).
[12] T. Peacock and G. Haller, "Lagrangian coherent structures: The hidden skeleton of fluid flows," Phys. Today **66**(2), 41–47 (2013).
[13] M. J. Olascoaga and G. Haller, "Forecasting sudden changes in environmental pollution patterns," Proc. Natl. Acad. Sci. U.S.A. **109**(13), 4738–4743 (2012).
[14] M. R. Allshouse and T. Peacock, "Lagrangian based methods for coherent structure detection," Chaos **25**(9), 097617 (2015).
[15] F. J. Beron-Vera, M. J. Olascoaga, and P. Miron, "Building a Maxey–Riley framework for surface ocean inertial particle dynamics," Phys. Fluids **31**(9), 96602 (2019).
[16] C. Coulliette, F. Lekien, J. D. Paduan, G. Haller, and J. E. Marsden, "Optimal pollution mitigation in Monterey Bay based on coastal radar data and nonlinear dynamics," Environ. Sci. Technol. **41**(18), 6562–6572 (2007).
[17] A. Hadjighasem, M. Farazmand, D. Blazevski, G. Froyland, and G. Haller, "A critical comparison of Lagrangian methods for coherent structure detection," Chaos **27**(5), 053104 (2017).
[18] N. Raju and E. Meiburg, "Dynamics of small, spherical particles in vortical and stagnation point flow fields," Phys. Fluids **9**(2), 299–314 (1997).
[19] I. J. Benczik, G. Károlyi, I. Scheuring, and T. Tél, "Coexistence of inertial competitors in chaotic flows," Chaos **16**(4), 043110 (2006).
[20] D. Kularatne, E. Forgoston, and M. A. Hsieh, "Using control to shape stochastic escape and switching dynamics," Chaos **29**(5), 053128 (2019).
[21] T. Salam, D. Kularatne, E. Forgoston, and M. A. Hsieh, "*Adaptive sampling and energy efficient navigation in time-varying flows*," in *Autonomous Underwater Vehicles* (Institution of Engineering and Technology, 2020), pp. 493–537.
[22] G. You, T. Wong, and S. Leung, "Eulerian methods for visualizing continuous dynamical systems using Lyapunov exponents," SIAM J. Sci. Comput. **39**(2), A415–A437 (2017).
[23] G. Haller and G. Yuan, "Lagrangian coherent structures and mixing in two-dimensional turbulence," Physica D **147**(3-4), 352–370 (2000).
[24] M. A. Hsieh, E. Forgoston, T. W. Mather, and I. B. Schwartz, "*Robotic manifold tracking of coherent structures in flows*," in *2012 IEEE International Conference on Robotics and Automation* (IEEE, 2012), pp. 4242–4247.
[25] M. Ani Hsieh, H. Hajieghrary, D. Kularatne, C. R. Heckman, E. Forgoston, I. B. Schwartz, and P. A. Yecko, "*Small and adrift with self-control: Using the environment to improve autonomy*," in *Robotics Research: Volume 2* (Cham: Springer International Publishing, 2018), pp. 387–402.
[26] K. Mallory, M. A. Hsieh, E. Forgoston, and I. B. Schwartz, "Distributed allocation of mobile sensing swarms in gyre flows," Nonlinear Proc. Geophys. **20**(5), 657–668 (2013).
[27] M. A. Hsieh, K. Mallory, E. Forgoston, and I. B. Schwartz, "*Distributed allocation of mobile sensing agents in geophysical flows*," in *2014 American Control Conference* (IEEE, 2014), pp. 165–171.
[28] M. Michini, K. Mallory, D. Larkin, M. A. Hsieh, E. Forgoston, and P. A. Yecko, "*An experimental testbed for multi-robot tracking of manifolds and coherent structures in flows*," in *Dynamic Systems and Control Conference* (American Society of Mechanical Engineers, 2013), Vol. 56130, p. V002T32A002.
[29] M. Van Aartrijk and H. J. H. Clercx, "Vertical dispersion of light inertial particles in stably stratified turbulence: The influence of the Basset force," Phys. Fluids **22**(1), 013301 (2010).
[30] F. J. Beron-Vera, M. J. Olascoaga, and R. Lumpkin, "Inertia-induced accumulation of flotsam in the subtropical gyres," Geophys. Res. Lett. **43**(23), 12–228, https://doi.org/10.1002/2016GL071443 (2016).
[31] L. K. Clark, M. H. DiBenedetto, N. T. Ouellette, and J. R. Koseff, "Settling of inertial nonspherical particles in wavy flow," Phys. Rev. Fluids **5**(12), 124301 (2020).
[32] J. Peng and J. Dabiri, "Transport of inertial particles by Lagrangian coherent structures: Application to predator–prey interaction in jellyfish feeding," J. Fluid Mech. **623**, 75–84 (2009).
[33] F. Lekien, S. C. Shadden, and J. E. Marsden, "Lagrangian coherent structures in *n*-dimensional systems," J. Math. Phys. **48**(6), 065404 (2007).
[34] M. R. Allshouse and T. Peacock, "Refining finite-time Lyapunov exponent ridges and the challenges of classifying them," Chaos **25**(8), 087410 (2015).
[35] G. Haller and T. Sapsis, "Where do inertial particles go in fluid flows?" Physica D **237**(5), 573–583 (2008).
[36] M. R. Maxey and J. J. Riley, "Equation of motion for a small rigid sphere in a nonuniform flow," Phys. Fluids **26**(4), 883–889 (1983).
[37] J. H. Cartwright, U. Feudel, G. Károlyi, A. de Moura, O. Piro, and T. Tél, "*Dynamics of finite-size particles in chaotic fluid flows*," in *Nonlinear Dynamics and Chaos: Advances and Perspectives* (Heidelberg: Springer Berlin Heidelberg, 2010), pp. 51–87.
[38] M. Farazmand and G. Haller, "The Maxey–Riley equation: Existence, uniqueness and regularity of solutions," Nonlinear Anal.: Real World Appl. **22**, 98–106 (2015).
[39] M. Sudharsan, S. L. Brunton, and J. J. Riley, "Lagrangian coherent structures and inertial particle dynamics," Phys. Rev. E **93**(3), 033108 (2016).
[40] A. Babiano, J. H. E. Cartwright, O. Piro, and A. Provenzale, "Dynamics of a small neutrally buoyant sphere in a fluid and targeting in Hamiltonian systems," Phys. Rev. Lett. **84**(25), 5764 (2000).
[41] T. Günther and H. Theisel, "Backward finite-time Lyapunov exponents in inertial flows," IEEE Trans. Vis. Comput. Graph. **23**(1), 970–979 (2016).
[42] I. J. Benczik, Z. Toroczkai, and T. Tél, "Selective sensitivity of open chaotic flows on inertial tracer advection: Catching particles with a stick," Phys. Rev. Lett. **89**(16), 164501 (2002).
[43] J. Pedlosky, *Ocean Circulation Theory* (Springer, 1996).
[44] A. Provenzale, "Transport by coherent barotropic vortices," Annu. Rev. Fluid Mech. **31**(1), 55–93 (1999).
[45] F. J. Beron-Vera, M. J. Olascoaga, G. Haller, M. Farazmand, J. Triñanes, and Y. Wang, "Dissipative inertial transport patterns near coherent Lagrangian eddies in the ocean," Chaos **25**(8), 087412 (2015).

[46]G. Haller, A. Hadjighasem, M. Farazmand, and F. Huhn, "Defining coherent vortices objectively from the vorticity," J. Fluid Mech. **795**, 136–173 (2016).
[47]D. del Castillo-Negrete and P. J. Morrison, "Chaotic transport by Rossby waves in shear flow," Phys. Fluids A **5**(4), 948–965 (1993).
[48]P. S. Marcus, "Vortex dynamics in a shearing zonal flow," J. Fluid Mech. **215**, 393–430 (1990).
[49]I. I. Rypina, M. G. Brown, F. J. Beron-Vera, H. Koçak, M. J. Olascoaga, and I. A. Udovydchenkov, "On the Lagrangian dynamics of atmospheric zonal jets and the permeability of the stratospheric polar vortex," J. Atmos. Sci. **64**(10), 3595–3610 (2007).
[50]F. J. Beron-Vera, M. J. Olascoaga, M. G. Brown, H. Koçak, and I. I. Rypina, "Invariant-tori-like Lagrangian coherent structures in geophysical flows," Chaos **20**(1), 017514 (2010).
[51]Q. Ni, X. Zhai, X. Jiang, and D. Chen, "Abundant cold anticyclonic eddies and warm cyclonic eddies in the global ocean," J. Phys. Oceanogr. **51**(9), 2793–2806 (2021).
[52]Y. Uchiyama, Y. Suzue, and H. Yamazaki, "Eddy-driven nutrient transport and associated upper-ocean primary production along the Kuroshio," J. Geophys. Res.: Oceans **122**(6), 5046–5062, https://doi.org/10.1002/2017JC012847 (2017).
[53]A. M. Hogg, M. P. Meredith, D. P. Chambers, E. P. Abrahamsen, C. W. Hughes, and A. K. Morrison, "Recent trends in the Southern Ocean eddy field," J. Geophys. Res.: Oceans **120**(1), 257–267, https://doi.org/10.1002/2014JC010470 (2015).
[54]I. Frenger, N. Gruber, R. Knutti, and M. Münnich, "Imprint of Southern Ocean eddies on winds, clouds and rainfall," Nat. Geosci. **6**(8), 608–612 (2013).
[55]M. Branicki and S. Wiggins, "Finite-time Lagrangian transport analysis: Stable and unstable manifolds of hyperbolic trajectories and finite-time Lyapunov exponents," Nonlinear Proc. Geophys. **17**(1), 1–36 (2010).
[56]Coastal Observing Research and Development Center (CORDC), "HFRNet: Surface current mapping by HF radar," see https://cordc.ucsd.edu/projects/hfrnet/ (last accessed May 22, 2025).
[57]Y. LeCun, Y. Bengio, and G. Hinton, "Deep learning," Nature **521**(7553), 436–444 (2015).
[58]Z. Ghahramani, "Probabilistic machine learning and artificial intelligence," Nature **521**(7553), 452–459 (2015).
[59]M. Qraitem, D. Kularatne, E. Forgoston, and M. A. Hsieh, "Bridging the gap: Machine learning to resolve improperly modeled dynamics," Physica D **414**, 132736 (2020).
[60]T. Z. Jiahao, M. A. Hsieh, and E. Forgoston, "Knowledge-based learning of nonlinear dynamics and chaos," Chaos **31**(11), 111101 (2021).
[61]K. Yao, E. Forgoston, and P. Yecko, "Learning ocean circulation models with reservoir computing," Phys. Fluids **34**(11), 116604 (2022).